

1 **Global CO emissions and drivers of atmospheric CO trends constrained by**
2 **MOPITT satellite measurements**

3
4 Zhaojun Tang^{1,2}, Panpan Yang¹, Kazuyuki Miyazaki³, John Worden³, Helen Worden⁴, Daven
5 K. Henze⁵, Dylan B. A. Jones⁶ and Zhe Jiang^{1*}

6
7 ¹Institute of Surface–Earth System Science, School of Earth System Sciences, Tianjin
8 University, Tianjin, 300072, China.

9 ²School of Earth and Space Sciences, University of Science and Technology of China, Hefei,
10 Anhui, 230026, China.

11 ³Jet Propulsion Laboratory, California Institute of Technology, Pasadena, CA, 91009, USA.

12 ⁴Atmospheric Chemistry Observations and Modeling Laboratory, National Center for
13 Atmospheric Research, Boulder, CO, 80301, USA.

14 ⁵Department of Mechanical Engineering, University of Colorado, Boulder, CO, 80309, USA.

15 ⁶Department of Physics, University of Toronto, Toronto, ON, M5S 1A7, Canada.

16
17 *Correspondence to: Zhe Jiang (zhejiang@tju.edu.cn)

18
19
20 **Abstract**

21 Carbon monoxide (CO), an important atmospheric pollutant produced by incomplete
22 combustion and hydrocarbon oxidation, significantly affects atmospheric oxidation capacity
23 and air quality. Accurate quantification of its global emissions and the underlying driver behind
24 its atmospheric trends is essential for understanding changes in global atmospheric
25 environment. Using 20 years (2003-2022) of data from the Measurement of Pollution in the
26 Troposphere (MOPITT) instrument, we analyze changes in global CO emissions and
27 atmospheric concentrations by applying a four-dimensional variational (4D-Var) assimilation
28 framework within the GEOS-Chem adjoint model. A posteriori simulations show good
29 agreement with independent surface and aircraft measurements compared to a priori
30 simulations. Sensitivity analyses further confirm that inferred emissions remain robust against
31 uncertainties associated with satellite vertical sensitivity and variations in hydroxyl radical (OH)
32 concentrations. Our results indicate a substantial decline in global anthropogenic CO emissions
33 of 14-17% (approximately 85-110 Tg yr⁻¹) over the two-decade period, largely driven by

34 emission reductions in the United States, Europe, and eastern China. Biomass burning
35 emissions exhibited strong interannual variability, with recent increases in Northern
36 Hemisphere high-latitude forests; in particular, the intense 2021 wildfires substantially offset
37 the anthropogenic emission-driven decline in atmospheric CO over the Northern Hemisphere.
38 This study provides a comprehensive assessment of global CO emissions and the mechanisms
39 governing atmospheric CO trends, offering a scientific basis for integrated policies addressing
40 both air pollution and climate change.

41

42 **1. Introduction**

43 Carbon monoxide (CO) is a key atmospheric pollutant produced from incomplete
44 combustion and the oxidation of hydrocarbons. As the main sink for the hydroxyl radical (OH),
45 CO critically influences the oxidative capacity of the atmosphere (Zhao et al., 2020; Tan et al.,
46 2022), and is an important precursor for tropospheric ozone (Whaley et al., 2015; Hu et al.,
47 2024). With a chemical lifetime of approximately one to two months, CO is frequently
48 employed as a valuable tracer for elucidating variations in anthropogenic activities and biomass
49 burning, providing critical insights into the long-range transport of atmospheric constituents
50 (Tang et al., 2019; Buchholz et al., 2022; Smoydzin and Hoor, 2022). By modulating the
51 abundance of OH, changes in CO concentrations indirectly affect the atmospheric lifetime of
52 methane (CH₄). Furthermore, CO shares common combustion sources with major greenhouse
53 gases like CH₄ and carbon dioxide (Worden et al., 2017; Zheng et al., 2023). Accurate
54 quantification of global CO emissions and a clear understanding of the drivers behind its
55 atmospheric trends are therefore essential for formulating effective policies to address the
56 challenges of air quality and climate change.

57 The advent of long-term satellite measurements has revolutionized our ability to monitor
58 global CO distributions (Warner et al., 2013; Worden et al., 2013; Hedelius et al., 2021),

59 enabling a shift from short-term, regional emission estimates (Arellano et al., 2004; Heald et
60 al., 2004; Kopacz et al., 2010) to analyses of decadal-scale changes. Numerous studies have
61 leveraged these records to report substantial declines in anthropogenic CO emissions (Fortems-
62 Cheiney et al., 2011; Jiang et al., 2017; Miyazaki et al., 2020), especially across the Northern
63 Hemisphere, contributing to improved air quality. However, a critical and emerging challenge
64 is to disentangle the competing influences on atmospheric CO concentrations. While
65 anthropogenic emissions are generally decreasing, biomass burning emissions exhibit strong
66 interannual variability. Thus, an important unanswered question is to what extent the recent
67 intensification of wildfires, particularly in high-latitude forests (Jain et al., 2024; Jones et al.,
68 2024), is offsetting the gains achieved from anthropogenic emission reductions. This has
69 profound implications, as a rise in wildfire CO signals a concurrent rise in wildfire greenhouse
70 gas emissions, which could offset part of the gains achieved from reductions in anthropogenic
71 greenhouse gas emissions.

72 Constraining global emissions and robustly attributing observed concentration trends
73 require the application of sophisticated inverse modeling approaches. These methods, which
74 include ensemble-based techniques (e.g., the ensemble Kalman filter) and variational methods
75 (e.g., four-dimensional variational, 4D-Var, data assimilation), provide powerful frameworks
76 for optimizing emission estimates by reconciling model simulations with satellite
77 measurements, while accounting for complex atmospheric transport and chemistry (Müller et
78 al., 2018; Miyazaki et al., 2020; Jiang et al., 2025). Among these, the 4D-Var data assimilation,
79 implemented within chemical transport models like GEOS-Chem and its adjoint (Henze et al.,
80 2007), has been widely and successfully applied to constrain CO emissions (Kopacz et al.,
81 2010; Jiang et al., 2015b; Tang et al., 2023), owing to its strengths in handling nonlinear
82 constraints and providing computationally efficient gradients. However, long-term multi-
83 decadal trend analyses based on this system has often been hindered by limitations such as

84 inconsistent meteorological inputs across years and the use of outdated a priori emission
85 inventories (Jiang et al., 2017; Qu et al., 2022).

86 To address these limitations, we employ a recent extension of the GEOS-Chem adjoint
87 model (Tang et al., 2023) that features support for consistent MERRA-2 meteorological data
88 and modern emission inventories via the Harmonized Emissions Component (HEMCO)
89 (Keller et al., 2014; Lin et al., 2021). By assimilating MOPITT (Measurements of Pollution in
90 the Troposphere) CO retrievals from 2003 to 2022, this study aims to provide an analysis with
91 the following specific objectives: (1) to quantify the long-term evolution of global CO
92 emissions; (2) to attribute the observed trends in atmospheric CO concentrations to changes in
93 emissions and meteorological variations, in particular, the effect of biomass burning emissions
94 on atmospheric CO decline driven by anthropogenic reductions; and (3) to evaluate the
95 sensitivity of inferred emissions to uncertainties in satellite vertical sensitivity and OH
96 concentrations. By doing so, this work aims to improve the understanding of key drivers behind
97 atmospheric CO changes and offer a refined emission inventory to support future air quality
98 and climate policies.

99 The paper is structured as follows: Section 2 describes the methodology, including the
100 assimilation framework, observational data, and the design of assimilation experiments.
101 Section 3 presents the results on the long-term emission trends, the robustness tests, and the
102 attribution of concentration changes. Conclusions are provided in Section 4.

103

104 **2. Methodology and Data**

105 **2.1 Assimilation framework**

106 We utilize the adjoint of the GEOS-Chem model (version 35n) with extended support for
107 MERRA-2 meteorological data and HEMCO emission inventories. The analysis is conducted
108 at a horizontal resolution of $2^\circ \times 2.5^\circ$ with 47 vertical levels (MERRA-2) up to 0.01 hPa and

109 employs a CO-only simulation (tagged-CO mode), in which the chemical sink of CO is
110 linearized with archived monthly mean OH fields. Two types of archived OH fields are used
111 in this study: fixed monthly OH fields for 2013 from the GEOS-Chem full chemistry simulation
112 (Fisher et al., 2017), and variable monthly OH fields for 2005-2020 from the Tropospheric
113 Chemistry Reanalysis version 2 (TCR-2, Miyazaki et al. (2020)). The TCR-2 OH fields have
114 been validated against various aircraft observations and show generally good agreement
115 (Miyazaki et al., 2020). Fig. S2 (see the SI) shows global mean tropospheric OH concentrations
116 from TCR-2, demonstrating a slight increasing trend ($1.0 \pm 0.6 \times 10^3 \text{ molec cm}^{-3} \text{ yr}^{-1}$) in 2005-
117 2020.

118 The global default anthropogenic emission inventory is the CEDS-CMIP6 (Community
119 Emissions Data System) (Hoesly et al., 2018). Regional emissions are replaced as follows:
120 MIX (Li et al., 2017) over Asia, NEI 2016 (National Emissions Inventory) over the United
121 States, DICE_AFRICA and EDGARv4.3 over Africa, and APEI over Canada. The contribution
122 of co-emitted anthropogenic VOC sources is considered by scaling up anthropogenic CO
123 emissions by 11%. Biogenic emissions are simulated using the Model of Emissions of Gases
124 and Aerosols from Nature, version 2.0 (MEGANv2.0, Guenther et al. (2006)). CH₄ oxidation
125 source is considered by using a prescribed, spatially varying CH₄ field following the default
126 tagged-CO configuration (Fisher et al., 2017). The CO sources from both biogenic VOCs and
127 CH₄ oxidation are calculated online based on the assumption of instantaneous oxidation by OH
128 radicals. Biomass burning emissions are based on the Global Fire Emissions Database version
129 4 (GFED4, van der Werf et al. (2010)). For years beyond the end year of a specific inventory,
130 emissions from the last available year within that inventory's coverage were used to fill the
131 subsequent years. The distribution of the annual mean CO emissions from 2003 to 2022 is
132 shown in Figs. 1a-c. The annual global sources are 536.3 Tg yr⁻¹ from anthropogenic emissions,
133 312.5 Tg yr⁻¹ from biomass burning, and 623 Tg yr⁻¹ from the oxidation of biogenic VOCs.

134 The objective of the 4D-Var approach is to minimize the difference between simulations
135 and observations by minimizing the cost function (Henze et al., 2007):

$$136 \quad J(\mathbf{x}) = \sum_{i=1}^N (\mathbf{F}_i(\mathbf{x}) - \mathbf{z}_i)^T \mathbf{S}_{\Sigma}^{-1} (\mathbf{F}_i(\mathbf{x}) - \mathbf{z}_i) + \gamma (\mathbf{x} - \mathbf{x}_a)^T \mathbf{S}_a^{-1} (\mathbf{x} - \mathbf{x}_a) \quad (1)$$

137 where \mathbf{x} is the state vector of CO emissions, N is the number of observations distributed in
138 time over the assimilation period, \mathbf{z}_i are the MOPITT CO retrievals, and $\mathbf{F}(\mathbf{x})$ is the forward
139 model. Error estimates are assumed to be Gaussian: \mathbf{S}_{Σ} is the observational error covariance,
140 which combines a 10% uniform error and the MOPITT CO retrieval error covariance; and \mathbf{S}_a
141 is a priori error covariance. Here the combustion-related CO sources (fossil fuel, biofuel, and
142 biomass burning) and the oxidation source from biogenic VOCs are combined, with a uniform
143 a priori error of 50% assumed following previous studies (Jiang et al., 2013; Jiang et al., 2017).
144 The CO source from CH₄ oxidation is optimized separately as an aggregated global source,
145 with a priori uncertainty of 25%. The cost function is minimized by iteratively adjusting the
146 CO emissions using the quasi-Newton gradient-based optimization L-BFGS-B algorithm (Zhu
147 et al., 1997) and the adjoint gradients:

$$148 \quad \nabla_{\mathbf{x}} J(\mathbf{x}) = \sum_{k=1}^N \left[2 \left(\frac{\partial \mathbf{F}_i}{\partial \mathbf{x}} \right)^T \mathbf{S}_{\Sigma}^{-1} (\mathbf{F}_i(\mathbf{x}) - \mathbf{z}_i) \right] + 2\gamma (\mathbf{x} - \mathbf{x}_a)^T \mathbf{S}_a^{-1} \quad (2)$$

149 The LOGX2 method (Jiang et al., 2015a; Jiang et al., 2017) is employed to improve the
150 reduction of negative gradients.

151 Following Jiang et al. (2017), we applied a two-step approach to mitigate the influence of
152 systematic biases in the model simulations. First, a sequential Kalman filter (Todling and Cohn,
153 1994; Tang et al., 2022) was used to assimilate MOPITT CO retrievals from October 1, 2002,
154 to December 31, 2022, providing optimized CO concentration fields with lower bias. As
155 illustrated in Fig. 2a, the GEOS-Chem model driven by the original monthly CO initial
156 conditions and a priori emission inventories (referred to as GC-original) substantially
157 underestimated column CO concentrations by approximately 30–40% (mean bias = $-39.4 \times$
158 10^{16} molec cm⁻²; Table 1). In contrast, simulations using the monthly CO initial conditions

159 derived from the sequential Kalman filter together with a priori emissions (GC-a priori) showed
160 markedly improved agreement with MOPITT CO retrievals (Fig. 2b), reducing the mean bias
161 to about 10% (mean bias = -9.7×10^{16} molec cm⁻²). Similarly, the use of optimized monthly
162 CO initial conditions led to considerable improvement in model performance against
163 independent surface and aircraft measurements (Table 1). The mean bias decreased from -18.3
164 ppb (GC-original) to -1.4 ppb (GC-a priori) for World Data Centre for Greenhouse Gases
165 (WDCGG) surface observations; from -18.9 ppb to -3.8 ppb for HIAPER Pole-to-Pole
166 Observations (HIPPO) aircraft data; and from -16.2 ppb to -3.4 ppb for Atmospheric
167 Tomography Mission (ATom) aircraft measurements. These results suggest that the substantial
168 negative biases seen in Fig. 2a largely originate from the accumulation of biases over preceding
169 months.

170 Furthermore, ocean scenes (pink grids in Fig. S3) were defined as land boundary
171 conditions. The optimized CO fields from the Kalman filter were used to update CO
172 concentrations over the ocean at hourly intervals during the forward simulation within the 4D-
173 Var process. Meanwhile, the 4D-Var system constrained CO emissions over land without
174 modifying oceanic CO distributions. As demonstrated by Jiang et al. (2017), the use of
175 optimized CO land boundary conditions in 4D-Var assimilation effectively reduces systematic
176 biases associated with long-range transport. By adopting this two-step assimilation framework,
177 the inversion focuses on optimizing fresh continental CO emissions, while reducing the
178 influence of uncertainties arising from transport and chemical processes, which tend to exhibit
179 larger systematic biases. Consequently, a posteriori CO emissions estimated in this study are
180 expected to be lower than those derived without adjustments to the initial and boundary CO
181 conditions. This reflects both the specific inverse modeling setup and a possible
182 underestimation in our a posteriori emission estimates, attributable to the emphasis on
183 constraining fresh continental CO sources.

184 Based on this assimilation framework, three sets of CO emission inversion experiments
185 are designed:

186 (1) Column-FixOH: uses MOPITT CO column concentration data with default OH fields
187 fixed in 2013.

188 (2) Profile-FixOH: uses MOPITT CO profile data with default OH fields fixed in 2013.

189 (3) Column-VarOH: uses MOPITT CO column concentration data with variable OH fields
190 from the TCR-2 tropospheric chemistry reanalysis.

191 By comparing the results of Column-FixOH and Profile-FixOH, the influence of different
192 MOPITT CO data types on CO source estimates can be assessed. Similarly, comparing
193 Column-FixOH and Column-VarOH allows for evaluation of the impact of different OH fields
194 on CO source estimates.

195 **2.2 MOPITT CO retrievals**

196 The MOPITT instrument was launched on December 18, 1999, aboard the NASA Terra
197 spacecraft. The satellite follows a sun-synchronous polar orbit at 705 km altitude, crossing the
198 equator at 10:30 local time. The instrument made measurements over a 612 km cross-track
199 scan, with a footprint of 22 km \times 22 km. The MOPITT data used in this study are from the
200 joint retrieval (version 9J) of CO, which combines thermal infrared (TIR, 4.7 μ m) and near-
201 infrared (NIR, 2.3 μ m) radiances using an optimal estimation approach (Worden et al., 2010;
202 Deeter et al., 2022). The retrieved volume mixing ratios are reported as layer averages across
203 10 pressure levels (surface, 900, 800, 700, 600, 500, 400, 300, 200, and 100 hPa). The
204 relationship between the retrieved CO profile and the true atmospheric state is expressed as:

$$205 \quad \hat{\mathbf{z}} = \mathbf{z}_a + \mathbf{A}(\mathbf{z} - \mathbf{z}_a) + \mathbf{G}\boldsymbol{\epsilon} \quad (3)$$

206 where \mathbf{z}_a is the MOPITT a priori CO profile, \mathbf{z} is the true atmospheric state, $\mathbf{G}\boldsymbol{\epsilon}$ represents
207 the retrieval error, and $\mathbf{A} = \partial\hat{\mathbf{z}}/\partial\mathbf{z}$ is the MOPITT averaging kernel matrix, indicating the
208 sensitivity of the retrieval to the actual atmospheric CO. We only consider data with Cloud

209 Description = 2 (cloud free) and exclude MOPITT data with CO column amounts less than
210 5×10^{17} molec cm^{-2} . The threshold (5×10^{17} molec cm^{-2}) was selected to prevent the influence of
211 certain potentially inaccurate, extremely low-concentration observations, which may also have
212 low observation errors in the cost function, on the 4D-Var assimilation (Jiang et al., 2013; Jiang
213 et al., 2017). Since the NIR channel relies on reflected solar radiation, only daytime data are
214 considered (Worden et al., 2010; Tang et al., 2024).

215 **2.3 Aircraft and surface CO measurements**

216 The HIPPO (Wofsy and HIPPO Science Team (2011)) were conducted using the
217 Gulfstream V aircraft from 2009 to 2011. The flights primarily covered the Pacific Ocean,
218 spanning latitudes from 67°S to 87°N, with continuous sampling from 0.2 to 12 km altitude.
219 The ATom (Wofsy and Atom Science Team (2018)) used the DC-8 aircraft from 2016 to 2018.
220 ATom covered similar altitude and latitudinal ranges as HIPPO but with broader spatial
221 coverage, particularly over the Atlantic Ocean. For HIPPO, a total of 687 CO profiles from
222 five missions were used directly. For ATom, CO measurements during continuous ascents and
223 descents were used to construct 523 CO profiles from four missions. Surface CO measurements
224 from the WDCGG are also included in this analysis. The WDCGG, operated by the Japan
225 Meteorological Agency under the World Meteorological Organization's Global Atmosphere
226 Watch (GAW) program, collects, archives, and distributes atmospheric greenhouse gas data,
227 including CO, contributed by various institutions worldwide.

228

229 **3. Results and Discussion**

230 **3.1 Evaluation of assimilation system performance**

231 Before presenting the estimated emission trends, we first evaluate the performance of our
232 assimilation system. The evaluation involves comparing modeled CO concentrations from the
233 GC-original, GC-a priori, and a posteriori simulations (Column-FixOH, Profile-FixOH,

234 Column-VarOH) over the period 2003-2022 against MOPITT satellite measurements, as well
235 as independent surface observations from WDCGG and aircraft measurements from HIPPO
236 and ATom. As summarized in Table 1, a posteriori simulations exhibit mean biases relative to
237 MOPITT retrievals ranging from -5.1 to -7.3×10^{16} molec cm^{-2} . These values are notably
238 smaller than the biases in the GC-a priori simulation (-9.7×10^{16} molec cm^{-2}) and the GC-
239 original simulation (-39.4×10^{16} molec cm^{-2}). Similarly, for the HIPPO aircraft observations,
240 a posteriori simulations show mean biases between -2.5 and -2.1 ppb, improved compared to
241 the GC-a priori (-3.8 ppb) and GC-original (-18.9 ppb) simulations. For ATom aircraft data, a
242 posteriori mean biases range from -2.9 to -1.6 ppb, also lower than those from the GC-a priori
243 (-3.4 ppb) and GC-original (-16.2 ppb) simulations. In the case of surface CO concentrations,
244 a posteriori simulations yield mean biases between 0.3 and 1.9 ppb relative to WDCGG
245 observations (Table 1), which are reduced compared to GC-original (-18.3 ppb) simulations,
246 and comparable with the GC-a priori (-1.4 ppb) simulations. A posteriori simulations slightly
247 overestimate surface concentrations relative to WDCGG data, while underestimating CO in the
248 free troposphere according to MOPITT and aircraft measurements. This systematic
249 discrepancy may be attributable to uncertainties in convective transport parameterizations
250 within the model.

251 Overall, the good consistency between a posteriori simulations and multiple independent
252 observation platforms demonstrates the capability of our assimilation system to effectively
253 constrain CO emissions. Given this confidence in the system's performance, we now present
254 the central findings of this study: the long-term evolution of CO emissions. As mentioned in
255 Section 2.1, the combustion-related CO sources and the oxidation source from biogenic VOCs
256 are combined, and thus, the inverse system optimizes total CO emissions within each model
257 grid cell. The subsequent attribution of emissions to specific source types (e.g., anthropogenic,
258 biomass burning) in an individual grid cell is based on the relative contribution of each source

259 category from a priori emission inventories. Specifically, a posteriori emission for a given
260 source type in a grid cell is calculated by applying the grid-scale scaling factor (the ratio of a
261 posteriori to a priori total emissions) to the corresponding a priori emission of that source type.
262 Different sources can finally be calculated because each source category possesses distinct
263 spatial patterns and seasonal variations.

264

265 **3.2 Long-term evolution of global CO emissions**

266 **3.2.1 Anthropogenic CO emissions**

267 At the global scale, anthropogenic CO emissions based on three inversion configurations
268 are estimated to be 7-14% higher than a priori values (Table 2) in 2003-2022 and show a clear
269 declining trend (Fig. 3f). Under the Column-FixOH configuration, global anthropogenic
270 emissions from 2003 to 2022 ranged from 546.1 to 654.1 Tg yr⁻¹, with a multi-year average of
271 approximately 610 Tg yr⁻¹ and a total reduction of about 17%; similar emission ranges and
272 reduction rates (14-17%) were obtained under the Profile-FixOH and Column-VarOH
273 configurations. These results are broadly consistent with Zheng et al. (2019). The
274 CEDS-CMIP7 inventory (Hoesly et al., 2018) shows significantly lower global CO emissions
275 than those derived from inverse modeling, though its decreasing trend is comparable. As shown
276 in Fig. 4a, negative trends (blue) were concentrated in three major industrialized regions:
277 eastern North America, Europe, and eastern China, forming a "reduction belt". These regions
278 accounted for over 65% of global anthropogenic CO emissions, and their systematic reductions
279 constituted the principal driver of the global downward trend. In contrast, positive trends (red)
280 were primarily distributed in northern India (increases of 15.2-22.3%) and Central Africa,
281 corresponding to rapid urbanization and industrialization processes.

282 In the United States (US), emissions declined rapidly from 2003 to 2009, followed by a
283 period of slower reduction (Fig. 3a). Over the entire period (2003-2022), US CO emissions

284 decreased at rates of 2.0-2.2 Tg yr⁻¹, resulting in a cumulative reduction of 46-49% (Table S1).
285 This phased reduction pattern is consistent with the diminishing marginal effects of widespread
286 transportation control technologies, as supported by independent studies (Elguindi et al., 2020;
287 Miyazaki et al., 2020). Our estimated emission magnitude and decreasing trend are similar to
288 Zheng et al. (2019) and the CEDS-CMIP7 in the US. European CO emissions (Fig. 3b)
289 followed a similar pattern (cumulative reduction of 32–34% over 2003-2022). Estimated
290 emissions over Europe in Zheng et al. (2019) are substantially higher than ours and show
291 stronger interannual variability. In comparison, the CEDS-CMIP7 inventory shows good
292 agreement with our results during 2003-2017, but a faster decline after 2017; and Fortems-
293 Cheiney et al. (2024) suggests continuous decline in CO emissions in Europe in 2011-2021.
294 This discrepancy could be possibly attributable to differences in the processing of initial and
295 boundary CO conditions (e.g., the use of climatological CO concentrations in Fortems-Cheiney
296 et al. (2024)).

297 The evolution of eastern China's CO emissions can be divided into four stages (Fig. 3c):
298 (1) a slight growth until 2007, peaking around that time; (2) a sharp decline of approximately
299 7% during the 2008 global financial crisis; (3) a temporary rebound from 2008 to 2010 under
300 economic stimulus policies; and (4) a continuous decline phase after 2010. From 2003 to 2022,
301 anthropogenic CO emissions from eastern China decreased at an average rate of 3.0-4.0 Tg yr⁻¹
302 (Table 2), with a cumulative reduction of 23-32% (Table S1). Zhao et al. (2012) and Xia et
303 al. (2016) confirmed the trend reversal around 2007, attributing it to improved energy
304 efficiency and strengthened emission controls, while Lin and McElroy (2011) and Tong et al.
305 (2016) highlighted the suppressive impact of the 2008 economic recession. Both Zheng et al.
306 (2019) and the CEDS-CMIP7 emission dataset show a declining trend consistent with our
307 results, although their emission magnitudes are lower. During 2019-2022, the emission
308 reduction rate accelerated to 4.8-8.3 Tg yr⁻¹, reflecting not only the short-term impact of the

309 COVID-19 pandemic but also the long-term cumulative effects of clean air policies and energy
310 structure transformation.

311 India exhibited a continuous growth in anthropogenic CO emissions from 2003 to 2009,
312 followed by a period of slower increase, with an average annual increase of 0.5-0.8 Tg yr⁻¹ in
313 2003-2022. Our estimated emission magnitude and trend are similar to Zheng et al. (2019) in
314 India. In comparison, the CEDS-CMIP7 inventory shows a similar trend, but its emission levels
315 are lower than those derived from inverse modeling. In Southeast Asia, anthropogenic CO
316 emissions exhibited a relatively stable and slow upward trend over the study period, though a
317 noticeable decline occurred from 2019 to 2022, which is likely associated with the impact of
318 the COVID-19 pandemic. The emission trend derived from our inversion is generally
319 consistent with that reported by Zheng et al. (2019) for this region, although their estimates
320 show stronger interannual variability. Compared with the CEDS-CMIP7 inventory, the trend
321 in CO emissions is similar to our results, but the emission magnitude in CEDS-CMIP7 is lower
322 than that derived from inverse modeling.

323 **3.2.2 Biomass burning CO emissions**

324 Globally, biomass burning CO emissions were 4-11% higher than a priori estimate in
325 2003-2022 (Table 3) and reached a historical peak of approximately 500 Tg yr⁻¹ in 2021 (Fig.
326 5g). In contrast to the clear decline of anthropogenic emissions, the trend in global biomass
327 burning CO emissions remains insignificant (Table 3). A comparison with the GFED5 emission
328 inventory (van der Werf et al., 2025) reveals noticeable differences: GFED5 estimates are
329 generally higher than our results (Fig. 5g), and do not show the 2021 peak. Spatial analysis
330 revealed a pronounced latitudinal differentiation in the changes of biomass burning CO
331 emissions (Figs. 4d-f): positive trends (red) were concentrated in Northern Hemisphere high-
332 latitude coniferous forests, while negative trends (blue) dominated tropical and subtropical
333 regions. This pattern is consistent with the "global fire emission geographic reconstruction"

334 observed by Zheng et al. (2023), reflecting the differential impacts of climate change across
335 latitudinal zones.

336 Emissions from high-latitude coniferous forests have shown different long-term trends
337 between boreal North America and boreal Asia over the past two decades (Figs. 5a-b). Peak
338 fire activity in boreal North America occurs during June-August (Fig. 6a); boreal Asia
339 experiences its primary fire season in June-August, with a secondary peak often observed in
340 March-May (Fig. 6b). When excluding the exceptional wildfire year of 2021, summertime
341 biomass burning CO emissions in boreal North America exhibited an overall declining trend
342 from 2003 to 2022 (Fig. 7a). In contrast, boreal Asia experienced a general increase in
343 summertime biomass burning CO emissions during the same period, even when 2021 is
344 omitted, though the trend is less pronounced than when including that extreme year (Fig. 7b).
345 The peak in wildfire emissions from high-latitude coniferous forests in 2021 was triggered by
346 severe, concurrent droughts across the Northern Hemisphere (Zheng et al., 2023). The
347 pronounced latitudinal amplification of emissions is consistent with higher carbon emission
348 density of boreal forests, which is 4-10 times greater than that of grasslands (Zheng et al., 2021).
349 GFED5 data suggests that boreal Asia's wildfire emissions peaked in 2012, different from
350 emission inversion results in this work and Zheng et al. (2023).

351 A notable decline in fire activity in South America occurred after 2010 (Fig. 5c),
352 particularly in August-September (Fig. 7c) coinciding with the peak wildfire season in South
353 America (Fig. 6c). The trend shift in CO emissions are consistent with the sharp reductions in
354 annual deforestation rates in the Brazilian Amazon from 25396 km² yr⁻¹ in 2003 to 7000 km²
355 yr⁻¹ in 2010 (Deeter et al., 2018). Africa experiences its primary fire season in June-September,
356 with a secondary peak often observed in December-February (Fig. 6d). Biomass burning CO
357 emissions in Africa exhibited a modest increasing trend overall (Fig. 5d), particularly in
358 February (Fig. 7c). Pronounced regional differentiation occurred, with increases in central

359 Africa and decreases in surrounding areas (Figs. 4d–f), reflecting the "strong contrast" pattern
360 described by Andela et al. (2017). Compared to the GFED5 inventory, our inversion results
361 generally show lower CO emission intensities.

362 Peak fire activity in Australia occurs during August-December (Fig. 6f); Southeast Asia
363 experiences its primary fire season in August-October, with a secondary peak often observed
364 in February-March (Fig. 6e). Emission patterns in Southeast Asia (Fig. 5e) and Australia (Fig.
365 5f) highlighted their sensitivity to large-scale climate oscillations. Major fire events in
366 Indonesia in 2006, 2009, 2015, and 2019 were closely linked to El Niño-induced droughts
367 (Page, 2009; Field et al., 2016). Australia's extreme fires in 2019 resulted from compound
368 extreme climate conditions influenced by the El Niño-Southern Oscillation, the Southern
369 Annular Mode, and the Indian Ocean Dipole (Deb et al., 2020). Building upon the observed
370 sensitivity to large-scale climate oscillations, the long-term interannual trend of wildfire
371 emissions across Southeast Asia and Australia remains insignificant, despite decline in August-
372 October in Southeast Asia (Fig. 7e) and September-November in Australia (Fig. 7f). Our
373 emission inversion shows lower CO emissions than GFED5 inventory in Southeast Asia and
374 Australia.

375 **3.2.3 Difference between combustion and biogenic NMVOC sources**

376 CO from combustion sources in the Northern Hemisphere showed strong regional
377 differentiation (Fig. 4), reflecting a dynamic redistribution between declining anthropogenic
378 sources and increasing biomass burning sources. Positive trends were densely distributed in
379 high-latitude regions, mainly due to increases in wildfires; Negative trends dominated mid-to-
380 low latitude industrialized areas. Tropical regions showed a mixed pattern, while the Southern
381 Hemisphere exhibited generally weaker trends. This spatial heterogeneity confirms a net global
382 decrease in combustion-related CO, revealing a clear contrast between increases at high
383 northern latitudes and decreases at mid-latitudes, reflecting the compound influences of

384 industrialization, policy interventions and climate change.

385 In contrast, CO produced from the oxidation of biogenic VOCs remained relatively stable
386 from 2003 to 2022 (Figs. 4g-i). This stability aligns with findings by Messina et al. (2016),
387 suggesting that global-scale biogenic VOC emissions are less sensitive to short-term climate
388 and land cover changes. The global stability of biogenic VOC-derived CO is important for
389 atmospheric chemistry, as these compounds are key reactants for OH radicals and play a
390 regulatory role in atmospheric oxidation capacity. This stable background provides a crucial
391 baseline for understanding changes in atmospheric oxidation processes. The weaker trends
392 compared to those reported by Jiang et al. (2017) may be associated with our use of continuous
393 MERRA-2 meteorological data, which enhances consistency in long-term analysis.

394

395 **3.3 Long-term evolution and drivers of global CO concentrations**

396 Building on the emission estimates evaluated above, this section investigates their ultimate
397 influence in the atmosphere by analyzing the spatiotemporal patterns and trends of CO
398 concentrations. We first present the mean state and long-term changes in CO concentrations,
399 and then quantitatively attribute these changes to their underlying drivers: emissions and
400 meteorology. Figs. 8a-c show the mean surface CO concentrations in 2003-2022 from a
401 posteriori simulations and WDCGG surface observations. Higher CO concentrations are
402 evident in regions with strong anthropogenic emissions, such as East Asia, India, and Southeast
403 Asia, as well as in areas with significant biomass burning, i.e., Central Africa and South
404 America. The long-term trends in surface CO (Figs. 8d-f) reveal declining concentrations over
405 North America, Europe, East Asia, and South America, which contrast with rising trends over
406 India, Boreal Asia, Central Africa, and Australia. The 20-year mean CO columns (Figs. 9a-c)
407 show a consistent spatial pattern, with the highest column concentrations over East Asia and
408 Central Africa, followed by South America, India, and Southeast Asia. In contrast, the long-

409 term trend of CO columns (Figs. 9d-f) exhibits a more uniform decrease across the Northern
410 Hemisphere, lacking the distinct regional hotspots observed in the surface trends. This suggests
411 that changes in CO are more thoroughly mixed within the column.

412 To quantitatively attribute the concentration trends to specific drivers, we conducted a
413 series of sensitivity experiments. The experimental design isolates the influence of individual
414 emission sectors by building a baseline scenario in which all emissions are fixed at 2003 levels
415 to reflect the impact of meteorological condition changes in 2003-2022. Three more sensitivity
416 experiments were then conducted in 2003-2022 in which only one emission category, i.e.,
417 anthropogenic, biomass burning, or biogenic VOC emissions, was allowed to vary over time,
418 respectively. The time-varying emissions in these sensitivity experiments were prescribed from
419 the Column-FixOH a posteriori inversion.

420 The results indicate that meteorological influences induced positive trends in surface CO
421 concentrations in regions such as central Africa, Southeast Asia, and the Tibetan Plateau (0.6-
422 1.8% yr⁻¹), along with slight negative trends in areas such as South America (Fig. 10a). The
423 meteorological impact on CO column concentrations was comparatively weaker (Fig. 10b),
424 showing positive trends of 0.45% yr⁻¹ over central Africa and the Tibetan Plateau. This vertical
425 differentiation implies that meteorological influences may primarily alter the vertical
426 distribution of CO through changes in convective transport, with a more limited effect on larger
427 horizontal scales. The derived meteorological impact is noticeably weaker than that reported
428 by Jiang et al. (2017), a discrepancy likely attributable to our use of consistent MERRA-2
429 meteorological fields, which enhances the reliability of the long-term trend analysis. Similarly,
430 the impact of biogenic VOC changes on CO concentrations (Figs. 10g, 10h) was markedly
431 weaker than in Jiang et al. (2017).

432 Anthropogenic emission changes were identified as the principal driver behind declining
433 CO levels, inducing strong negative trends in industrial regions of the Northern Hemisphere,

434 such as eastern North America, Europe, and eastern China. This signal is consistent across both
435 surface and column concentrations (Figs. 10c-d). Globally, anthropogenic emission changes
436 led to an average annual decrease of $0.27\% \text{ yr}^{-1}$ in CO column concentrations, with a more
437 pronounced decline rate of $0.51\% \text{ yr}^{-1}$ in the Northern Hemisphere (Table 4). Regionally, the
438 US, Europe, and eastern China exhibited the most substantial decreases, at $-0.57\% \text{ yr}^{-1}$, -0.69%
439 yr^{-1} and $-0.69\% \text{ yr}^{-1}$, respectively. In contrast, India experienced a slight concentration increase
440 ($0.03\% \text{ yr}^{-1}$) due to rising emissions, while Southeast Asia showed a more moderate decline ($-$
441 $0.19\% \text{ yr}^{-1}$) compared to other major industrial regions.

442 Conversely, changes in biomass burning emissions generally contributed to positive trends
443 in CO, particularly at high latitudes (Figs. 10e-f). At global and Northern Hemispheric scales,
444 this positive trend was largely attributable to extreme wildfire activity in 2021. When 2021 is
445 excluded, the long-term trend in CO columns due to biomass burning becomes statistically
446 insignificant at these broad scales (Figs. 7g-h), with only regionally and seasonally confined
447 increases remaining apparent, notably over Boreal Asia (July-August, Fig. 7b) and Africa
448 (January-April, Fig. 7d). In the full record (including 2021), biomass burning emissions led to
449 an average annual increase of $0.10\% \text{ yr}^{-1}$ in global CO columns, and $0.24\% \text{ yr}^{-1}$ in the Northern
450 Hemisphere (Table 4). It is noteworthy that the CO concentration response lagged behind
451 emission pulses by about one month and persisted longer. In the Northern Hemisphere, for
452 instance, enhanced emissions occurred mainly from July to September, whereas the significant
453 concentration response extended from August to December (Fig. 7g). This lag and prolonged
454 influence were primarily attributable to the delayed response over Boreal North America (Fig.
455 7a). At the regional scale, increases occurred in Boreal North America ($0.43\% \text{ yr}^{-1}$) and Boreal
456 Asia ($0.48\% \text{ yr}^{-1}$). In contrast, South America, Australia, and Southeast Asia experienced
457 declining trends ranging from $-0.13\% \text{ yr}^{-1}$ to $-0.22\% \text{ yr}^{-1}$, while Africa showed a slight increase
458 of $0.09\% \text{ yr}^{-1}$.

459 This attribution analysis highlights the substantial impact of extreme wildfire years on the
460 CO budget. Although anthropogenic emission reductions lowered Northern Hemisphere CO
461 columns by approximately $0.51\% \text{ yr}^{-1}$, the intense biomass burning emissions in 2021
462 introduced a positive perturbation of about $0.24\% \text{ yr}^{-1}$ in the full-record trend, thereby offsetting
463 a considerable fraction of the anthropogenic-driven decline. As a result, the net concentration
464 decline was reduced to approximately $0.27\% \text{ yr}^{-1}$ in the analysis including 2021. This implies
465 that nearly half (47%) of the potential air quality improvement from anthropogenic emission
466 controls can be offset by wildfire emissions. This finding provides a clear mechanistic
467 explanation for the decline in atmospheric CO concentrations in recent years, and underscores
468 the growing role of extreme wildfire events in modulating regional to hemispheric air
469 composition.

470

471 **3.4 Impacts of systematic errors on inferred CO emissions**

472 The MOPITT instrument provides retrievals for both CO total column and vertical profile.
473 The degrees of freedom for signal (DFS) for MOPITT multi-spectral profile retrievals
474 (TIR+NIR) is approximately 1.5-2.0 over land, reducing to about 1.0 when converted to a total
475 column (Worden et al., 2010). The discrepancy between a posteriori emission estimates
476 constrained by CO column (Column-FixOH) and profile (Profile-FixOH) data helps evaluate
477 the influence of systematic errors associated with the vertical sensitivity of the satellite
478 retrievals (Tang et al., 2024). Globally, a posteriori anthropogenic and biomass burning CO
479 emissions from Profile-FixOH were both slightly lower than those from Column-FixOH, with
480 average differences of -6.6% and -5.5%, respectively, over the period 2003-2022 (Table 2).
481 The two configurations also showed broadly consistent long-term trends in inferred
482 anthropogenic emissions, both indicating a global decline of approximately $-0.9\% \text{ yr}^{-1}$. Larger
483 regional discrepancies were observed over eastern China ($-2.1\% \text{ yr}^{-1}$ for Profile-FixOH vs. -

484 1.6% yr⁻¹ for Column-FixOH) and India (1.1% yr⁻¹ vs. 0.7% yr⁻¹). Similarly, the trends in global
485 biomass burning CO emissions were consistent (0.3% yr⁻¹ for Column-FixOH and 0.5% yr⁻¹
486 for Profile-FixOH), though regional differences were more pronounced for boreal North
487 America (3.1% yr⁻¹ vs. 4.9% yr⁻¹) and Australia (-1.5% yr⁻¹ vs. -0.7% yr⁻¹). The limited
488 differences in inferred emissions between the two configurations resulted in a consistent
489 declining trend in simulated CO columns (-0.5% yr⁻¹ for both).

490 OH concentrations in model simulations significantly influence the inverse analysis of CO
491 emissions (Jiang et al., 2011; Müller et al., 2018). By assimilating MOPITT CO column data,
492 we compared the inverted CO emission estimates driven by fixed (Column-FixOH) and
493 variable (Column-VarOH) OH fields to investigate the potential influence. As shown in Fig.
494 11c, OH concentrations from the TCR-2 reanalysis are broadly 10-40% lower than the fixed
495 climatological OH concentrations over land (differences over the ocean are not considered here
496 due to the use of CO land boundary conditions in the 4D-Var assimilation). Lower OH
497 concentrations over land lead to reduced chemical loss, which is compensated by lower global
498 anthropogenic CO emissions in Column-VarOH inversion (590.1 Tg yr⁻¹) in 2003-2022,
499 approximately 3.7% lower than in Column-FixOH (612.8 Tg yr⁻¹).

500 Variations in OH concentrations influence the oxidation of biogenic VOCs to CO and their
501 subsequent chemical loss. These two counteracting processes establish a complex balance,
502 ultimately reflected in the inverted estimates of biogenic CO sources. Specifically, the Column-
503 VarOH inversion yields an average global biogenic CO sources of 391.4 Tg yr⁻¹ in 2003-2022,
504 approximately 3.9% lower than the 407.6 Tg yr⁻¹ in Column-FixOH inversion. The sensitivity
505 experiments described above address the third objective of this study, which is to evaluate the
506 robustness of our central findings against potential systematic errors associated with satellite
507 retrieval vertical sensitivity and OH concentrations. This robustness can be attributed, in part,
508 to our two-step inversion framework, which mitigates systematic biases through optimized

509 initial and boundary CO conditions.

510

511 **4. Conclusions**

512 This study provides a comprehensive, quantitative analysis of global CO emissions and
513 drivers governing atmospheric CO trends over the past two decades (2003-2022). By
514 employing a 4D-Var assimilation framework within GEOS-Chem adjoint model, constrained
515 by long-term MOPITT satellite measurements, we have generated an observationally
516 constrained CO emission inventory. A central methodological strength lies in the use of
517 continuous MERRA-2 meteorological fields and modern a priori emission inventories, which
518 significantly enhanced the long-term consistency and reliability of our trend analysis. The
519 implementation of a two-step bias mitigation strategy, optimizing both initial conditions and
520 land boundary conditions for CO, effectively reduced the accumulated impacts of transport and
521 chemistry uncertainties. The optimized emissions yield simulated CO concentrations that show
522 good agreement with independent surface measurements from the WDCGG network and
523 aircraft-based profiles from the HIPPO and ATom campaigns. The mean bias in simulated CO
524 concentrations (model minus observation) was reduced from -3.8 ppb in a priori simulation to
525 between -2.5 and -2.1 ppb in a posteriori simulation for HIPPO, and from -3.4 ppb in a priori
526 simulation to between -2.9 and -1.6 ppb in a posteriori simulation for ATOM.

527 Our results demonstrate a significant 14-17% decline (approximately 85-110 Tg yr⁻¹) in
528 global anthropogenic CO emissions over the 20-year period. This reduction was predominantly
529 driven by pollution control policies in major industrialized regions, with cumulative reductions
530 of 46-49% in the US, 32-34% in Europe, and 23-32% in eastern China. The decline in
531 anthropogenic CO emissions is consistent with the trends reported in the CEDS-CMIP7
532 inventory and the inversion results of Zheng et al. (2019), and is identified as the dominant and
533 statistically significant driver behind the observed decrease in atmospheric CO concentrations.

534 For biomass burning, our emission estimates suggested the historical peak of approximately
535 500 Tg yr⁻¹ in 2021, while the overall CO emissions in GFED5 inventory are higher than our
536 estimates in 2003-2022. Biomass burning emissions exhibited strong interannual variability
537 without a statistically significant long-term trend at the global and Northern Hemispheric scales,
538 although regionally and seasonally trends, such as in the boreal Northern Hemisphere during
539 summer, were evident in certain periods.

540 A central finding of this work is the substantial impact of extreme wildfire events,
541 particularly the record-breaking 2021 burning season in Northern Hemisphere high latitudes.
542 Our attribution analysis reveals that these wildfires introduced a strong positive perturbation to
543 atmospheric CO, offsetting nearly half (47%) of the concentration decline driven by
544 anthropogenic reductions in the Northern Hemisphere over our study period (2003-2022). This
545 finding highlights that while not a persistent trend, extreme wildfire events can counteract a
546 large fraction of the gains achieved from decades of emission control efforts. Our analysis thus
547 clarifies the past evolution of global CO emissions and concentrations, highlighting an
548 increasingly critical challenge: climate change is amplifying the intensity and impact of
549 extreme wildfire events, which can periodically undermine emission control efforts. This
550 underscores the need for integrated policies that address both anthropogenic sources and the
551 climate-driven amplification of natural emissions.

552

553 **Code and data availability:** The MOPITT CO data can be downloaded from
554 <https://asdc.larc.nasa.gov/data/MOPITT/>. The adjoint of GEOS-Chem model can be
555 downloaded from http://wiki.seas.harvard.edu/geos-chem/index.php/GEOS-Chem_Adjoint. A
556 posteriori CO emission estimates (Column-FixOH, Profile-FixOH and Column-VarOH) can
557 be downloaded from <https://doi.org/10.5281/zenodo.17221834>.

558

559 **Author Contributions:** Z.J. designed the research. Z.T. developed the model code and
560 performed the research. Z.J. and Z.T. wrote the manuscript. All authors contributed to
561 discussions and editing the manuscript.

562

563 **Competing interests:** The authors declare that they have no conflicts of interest.

564

565 **Acknowledgments:** We thank the providers of the MOPITT CO data. This work was
566 supported by the National Natural Science Foundation of China (42277082). Part of this work
567 was conducted at the Jet Propulsion Laboratory, California Institute of Technology, under
568 contract with NASA.

569

570 **Tables and Figures**

571 **Table 1.** Mean biases of modeled CO concentrations relative to satellite (MOPITT) and in-situ
572 (WDCGG, HIPPO, AToM) observations for five model simulations over the period 2003-2022.
573 Biases are in units of 10^{16} molec cm^{-2} for MOPITT and ppb for other datasets.

574

575 **Table 2.** Mean anthropogenic CO emissions (Tg yr^{-1}) and their trends (Tg yr^{-2}) in 2003-2022:
576 A comparison of a priori inventories with those constrained by MOPITT retrievals under
577 different configurations. The region definition is shown in Figure S1e.

578

579 **Table 3.** Mean biomass burning CO emissions (Tg yr^{-1}) and their trends (Tg yr^{-2}) in 2003-
580 2022: A comparison of a priori inventories (GFED4) with those constrained by MOPITT
581 retrievals under different configurations. The region definition is shown in Figure S1f.

582

583 **Table 4.** Attribution of trends in column CO concentrations ($\% \text{ yr}^{-1}$) from 2003 to 2022 to
584 changes in anthropogenic and biomass burning emissions, based on sensitivity simulations
585 using the Column-FixOH inversion results.

586

587 **Fig. 1.** Spatial patterns of a priori CO emissions and a posteriori emission scaling factors for
588 the period 2003-2022. (a-c) Mean a priori CO emissions (10^{12} molec $\text{cm}^{-2} \text{ s}^{-1}$). (d-l) Scaling

589 factors (ratio of a posteriori to a priori emissions) derived from the three inversion experiments:
590 (d-f) Column-FixOH, (g-i) Profile-FixOH, and (j-l) Column-VarOH.

591

592 **Fig. 2.** Relative bias in column CO for 2003-2022, calculated as (Model - MOPITT) / MOPITT
593 for GC-original (a), GC-a priori (b), and a posteriori simulations (c-e).

594

595 **Fig. 3.** Time series of anthropogenic CO emissions from 2003 to 2022 across major regions,
596 comparing a priori inventories, a posteriori inversions from this study, and independent
597 estimates from CEDS-CMIP6/7 and Zheng et al. (2019).

598

599 **Fig. 4.** Long-term trends in CO emissions (10^{10} molec cm^{-2} s^{-1} yr^{-1}) from different sources
600 (2003-2022) as constrained by the three inversion experiments. For anthropogenic and biogenic
601 VOC trends, months dominated by biomass burning (>50% contribution) were excluded in this
602 figure. This approach ensures that the derived trends more accurately reflect the actual changes
603 in anthropogenic and biogenic VOC emissions, without being biased by short-term, seasonal
604 biomass burning signals.

605

606 **Fig. 5.** Time series of biomass burning CO emissions from 2003 to 2022, comparing the a priori
607 inventory (GFED4), a posteriori inversions, and the GFED5 inventory.

608

609 **Fig. 6.** Climatological monthly cycle (2003-2022 average) of biomass burning CO emissions
610 across different regions, comparing a priori (GFED4) and a posteriori estimates with GFED5.

611

612 **Fig. 7.** Monthly trends in biomass burning CO emissions (based on Column-FixOH) and their
613 impact on column CO concentrations (2003-2022). Solid lines show trends including 2021,
614 while dashed lines exclude 2021 to illustrate the impact of extreme fire year. Please check Fig.
615 S4 and S5 for the standard deviation of the trends.

616

617 **Fig. 8.** Modeled surface CO concentrations (ppb) and their trends ($\% \text{yr}^{-1}$) from 2003 to 2022.
618 (a-c) Mean concentrations from WDCGG observations and model simulations. (d-f) Spatial
619 pattern of the long-term trend. Only stations with 14 year observations (the time range between
620 the first and last observations) during 2003-2022 are included.

621

622 **Fig. 9.** Modeled column CO concentrations (10^{18} molec cm^{-2}) and their trends ($\% \text{ yr}^{-1}$) from
623 2003 to 2022. (a-c) Spatial distribution of the 20-year mean. (d-f) Spatial pattern of the long-
624 term trend.

625

626 **Fig. 10.** Attribution of trends ($\% \text{ yr}^{-1}$) in surface and column CO concentrations to individual
627 drivers, derived from sensitivity simulations based on Column-FixOH inversion (2003-2022).
628 Trends are shown for scenarios with: (a, b) all emissions fixed at 2003 levels; (c, d) only
629 anthropogenic emissions varying over time; (e, f) only biomass burning emissions varying; (g,
630 h) only biogenic VOC emissions varying.

631

632 **Fig. 11.** Sensitivity of inverted CO emissions to OH fields. (a-c) Tropospheric OH columns
633 (10^{12} molec cm^{-2}) from fixed and variable (TCR-2) fields and their difference. (d-f)
634 Corresponding scaling factors from the Column-FixOH and Column-VarOH inversions and
635 their difference. Please note that due to the use of land boundary conditions, differences in OH
636 concentrations over the ocean in the left column figures have a negligible effect on the
637 differences in scaling factors shown in the right column figures.

638

639 **References**

- 640 Andela, N., Morton, D. C., Giglio, L., Chen, Y., van der Werf, G. R., Kasibhatla, P. S., DeFries,
641 R. S., Collatz, G. J., Hantson, S., Kloster, S., Bachelet, D., Forrest, M., Lasslop, G., Li, F.,
642 Mangeon, S., Melton, J. R., Yue, C., and Randerson, J. T.: A human-driven decline in global
643 burned area, *Science*, 356, 1356-1362, 10.1126/science.aal4108, 2017.
- 644 Arellano, A. F., Kasibhatla, P. S., Giglio, L., van der Werf, G. R., and Randerson, J. T.: Top-
645 down estimates of global CO sources using MOPITT measurements, *Geophys. Res. Lett.*, 31,
646 L01104, 10.1029/2003gl018609, 2004.
- 647 Buchholz, R. R., Park, M., Worden, H. M., Tang, W., Edwards, D. P., Gaubert, B., Deeter, M.
648 N., Sullivan, T., Ru, M., Chin, M., Levy, R. C., Zheng, B., and Magzamen, S.: New seasonal
649 pattern of pollution emerges from changing North American wildfires, *Nat. Commun.*, 13,
650 2043, 10.1038/s41467-022-29623-8, 2022.
- 651 Deb, P., Moradkhani, H., Abbaszadeh, P., Kiem, A. S., Engström, J., Keellings, D., and
652 Sharma, A.: Causes of the Widespread 2019–2020 Australian Bushfire Season, *Earth's*
653 *Future*, 8, e2020EF001671, 10.1029/2020ef001671, 2020.
- 654 Deeter, M., Francis, G., Gille, J., Mao, D., Martínez-Alonso, S., Worden, H., Ziskin, D.,
655 Drummond, J., Commane, R., Diskin, G., and McKain, K.: The MOPITT Version 9 CO
656 product: sampling enhancements and validation, *Atmos. Meas. Tech.*, 15, 2325-2344,
657 10.5194/amt-15-2325-2022, 2022.

658 Deeter, M. N., Martínez-Alonso, S., Andreae, M. O., and Schlager, H.: Satellite-Based
659 Analysis of CO Seasonal and Interannual Variability Over the Amazon Basin, *J. Geophys.*
660 *Res.-Atmos.*, 123, 5641-5656, 10.1029/2018jd028425, 2018.

661 Elguindi, N., Granier, C., Stavrou, T., Darras, S., Bauwens, M., Cao, H., Chen, C., Denier
662 van der Gon, H. A. C., Dubovik, O., Fu, T. M., Henze, D. K., Jiang, Z., Keita, S., Kuenen, J.
663 J. P., Kurokawa, J., Liousse, C., Miyazaki, K., Müller, J. F., Qu, Z., Solmon, F., and Zheng,
664 B.: Intercomparison of Magnitudes and Trends in Anthropogenic Surface Emissions From
665 Bottom-Up Inventories, Top-Down Estimates, and Emission Scenarios, *Earth's Future*, 8,
666 e2020EF001520, 10.1029/2020ef001520, 2020.

667 Field, R. D., van der Werf, G. R., Fanin, T., Fetzer, E. J., Fuller, R., Jethva, H., Levy, R.,
668 Livesey, N. J., Luo, M., Torres, O., and Worden, H. M.: Indonesian fire activity and smoke
669 pollution in 2015 show persistent nonlinear sensitivity to El Niño-induced drought, *Proc.*
670 *Natl. Acad. Sci. USA*, 113, 9204-9209, 10.1073/pnas.1524888113, 2016.

671 Fisher, J. A., Murray, L. T., Jones, D. B. A., and Deutscher, N. M.: Improved method for linear
672 carbon monoxide simulation and source attribution in atmospheric chemistry models
673 illustrated using GEOS-Chem v9, *Geosci. Model Dev.*, 10, 4129-4144, 10.5194/gmd-10-
674 4129-2017, 2017.

675 Fortems-Cheiney, A., Chevallier, F., Pison, I., Bousquet, P., Szopa, S., Deeter, M. N., and
676 Clerbaux, C.: Ten years of CO emissions as seen from Measurements of Pollution in the
677 Troposphere (MOPITT), *J. Geophys. Res.-Atmos.*, 116, D05304, 10.1029/2010jd014416,
678 2011.

679 Fortems-Cheiney, A., Broquet, G., Potier, E., Plauchu, R., Berchet, A., Pison, I., Denier van
680 der Gon, H., and Dellaert, S.: CO anthropogenic emissions in Europe from 2011 to 2021:
681 insights from Measurement of Pollution in the Troposphere (MOPITT) satellite data, *Atmos.*
682 *Chem. Phys.*, 24, 4635-4649, 10.5194/acp-24-4635-2024, 2024.

683 Guenther, A., Karl, T., Harley, P., Wiedinmyer, C., Palmer, P. I., and Geron, C.: Estimates of
684 global terrestrial isoprene emissions using MEGAN (Model of Emissions of Gases and
685 Aerosols from Nature), *Atmos. Chem. Phys.*, 6, 3181-3210, 10.5194/acp-6-3181-2006, 2006.

686 Heald, C. L., Jacob, D. J., Jones, D. B. A., Palmer, P. I., Logan, J. A., Streets, D. G., Sachse,
687 G. W., Gille, J. C., Hoffman, R. N., and Nehr Korn, T.: Comparative inverse analysis of
688 satellite (MOPITT) and aircraft (TRACE-P) observations to estimate Asian sources of carbon
689 monoxide, *J. Geophys. Res.-Atmos.*, 109, D23306, 10.1029/2004jd005185, 2004.

690 Hedelius, J. K., Toon, G. C., Buchholz, R. R., Iraci, L. T., Podolske, J. R., Roehl, C. M.,
691 Wennberg, P. O., Worden, H. M., and Wunch, D.: Regional and urban column CO trends and
692 anomalies as observed by MOPITT over 16 years, *J. Geophys. Res.-Atmos.*, 126,
693 e2020JD033967, 10.1029/2020jd033967, 2021.

694 Henze, D. K., Hakami, A., and Seinfeld, J. H.: Development of the adjoint of GEOS-Chem,
695 *Atmos. Chem. Phys.*, 7, 2413-2433, 10.5194/acp-7-2413-2007, 2007.

696 Hoesly, R. M., Smith, S. J., Feng, L., Klimont, Z., Janssens-Maenhout, G., Pitkanen, T.,
697 Seibert, J. J., Vu, L., Andres, R. J., Bolt, R. M., Bond, T. C., Dawidowski, L., Kholod, N.,
698 Kurokawa, J.-i., Li, M., Liu, L., Lu, Z., Moura, M. C. P., O'Rourke, P. R., and Zhang, Q.:
699 Historical (1750–2014) anthropogenic emissions of reactive gases and aerosols from the

700 Community Emissions Data System (CEDS), *Geosci. Model Dev.*, 11, 369-408,
701 10.5194/gmd-11-369-2018, 2018.

702 Hu, W., Zhao, Y., Lu, N., Wang, X., Zheng, B., Henze, D. K., Zhang, L., Fu, T. M., and Zhai,
703 S.: Changing Responses of PM_{2.5} and Ozone to Source Emissions in the Yangtze River Delta
704 Using the Adjoint Model, *Environ. Sci. Technol.*, 58, 628-638, 10.1021/acs.est.3c05049,
705 2024.

706 Jain, P., Barber, Q. E., Taylor, S. W., Whitman, E., Castellanos Acuna, D., Boulanger, Y.,
707 Chavardès, R. D., Chen, J., Englefield, P., Flannigan, M., Girardin, M. P., Hanes, C. C., Little,
708 J., Morrison, K., Skakun, R. S., Thompson, D. K., Wang, X., and Parisien, M.-A.: Drivers
709 and Impacts of the Record-Breaking 2023 Wildfire Season in Canada, *Nat. Commun.*, 15,
710 6764, 10.1038/s41467-024-51154-7, 2024.

711 Jiang, Z., Jones, D. B. A., Kopacz, M., Liu, J., Henze, D. K., and Heald, C.: Quantifying the
712 impact of model errors on top-down estimates of carbon monoxide emissions using satellite
713 observations, *J. Geophys. Res.-Atmos.*, 116, D15306, 10.1029/2010jd015282, 2011.

714 Jiang, Z., Jones, D. B. A., Worden, H. M., Deeter, M. N., Henze, D. K., Worden, J., Bowman,
715 K. W., Brenninkmeijer, C. A. M., and Schuck, T. J.: Impact of model errors in convective
716 transport on CO source estimates inferred from MOPITT CO retrievals, *J. Geophys. Res.-
717 Atmos.*, 118, 2073-2083, 10.1002/jgrd.50216, 2013.

718 Jiang, Z., Jones, D. B. A., Worden, H. M., and Henze, D. K.: Sensitivity of top-down CO source
719 estimates to the modeled vertical structure in atmospheric CO, *Atmos. Chem. Phys.*, 15, 1521-
720 1537, 10.5194/acp-15-1521-2015, 2015a.

721 Jiang, Z., Jones, D. B. A., Worden, J., Worden, H. M., Henze, D. K., and Wang, Y. X.: Regional
722 data assimilation of multi-spectral MOPITT observations of CO over North America, *Atmos.
723 Chem. Phys.*, 15, 6801-6814, 10.5194/acp-15-6801-2015, 2015b.

724 Jiang, Z., Worden, J. R., Worden, H., Deeter, M., Jones, D. B. A., Arellano, A. F., and Henze,
725 D. K.: A 15-year record of CO emissions constrained by MOPITT CO observations, *Atmos.
726 Chem. Phys.*, 17, 4565-4583, 10.5194/acp-17-4565-2017, 2017.

727 Jiang, Z., Lin, J., He, T.-L., Jiang, F., Jin, J., Qin, K., Shen, L., Yang, P., Zang, Z., Zhang, L.,
728 Zhang, Y., Zheng, B., Zhong, H., and Zhu, L.: Satellite-Based Emission Inversion for Air
729 Pollutants and Greenhouse Gases: A Review, *J. Meteor. Res.*, 39, 1101-1125,
730 10.1007/s13351-025-4914-7, 2025.

731 Jones, M. W., Veraverbeke, S., Andela, N., Doerr, S. H., Kolden, C., Mataveli, G., Pettinari,
732 M. L., Le Quere, C., Rosan, T. M., van der Werf, G. R., van Wees, D., and Abatzoglou, J. T.:
733 Global rise in forest fire emissions linked to climate change in the extratropics, *Science*, 386,
734 ead15889, 10.1126/science.adl5889, 2024.

735 Keller, C. A., Long, M. S., Yantosca, R. M., Da Silva, A. M., Pawson, S., and Jacob, D. J.:
736 HEMCO v1.0: a versatile, ESMF-compliant component for calculating emissions in
737 atmospheric models, *Geosci. Model Dev.*, 7, 1409-1417, 10.5194/gmd-7-1409-2014, 2014.

738 Kopacz, M., Jacob, D. J., Fisher, J. A., Logan, J. A., Zhang, L., Megretskaia, I. A., Yantosca,
739 R. M., Singh, K., Henze, D. K., Burrows, J. P., Buchwitz, M., Khlystova, I., McMillan, W.
740 W., Gille, J. C., Edwards, D. P., Eldering, A., Thouret, V., and Nedelec, P.: Global estimates
741 of CO sources with high resolution by adjoint inversion of multiple satellite datasets

742 (MOPITT, AIRS, SCIAMACHY, TES), *Atmos. Chem. Phys.*, 10, 855-876, 10.5194/acp-10-
743 855-2010, 2010.

744 Li, M., Zhang, Q., Kurokawa, J.-i., Woo, J.-H., He, K., Lu, Z., Ohara, T., Song, Y., Streets, D.
745 G., Carmichael, G. R., Cheng, Y., Hong, C., Huo, H., Jiang, X., Kang, S., Liu, F., Su, H., and
746 Zheng, B.: MIX: a mosaic Asian anthropogenic emission inventory under the international
747 collaboration framework of the MICS-Asia and HTAP, *Atmos. Chem. Phys.*, 17, 935-963,
748 10.5194/acp-17-935-2017, 2017.

749 Lin, H., Jacob, D. J., Lundgren, E. W., Sulprizio, M. P., Keller, C. A., Fritz, T. M., Eastham,
750 S. D., Emmons, L. K., Campbell, P. C., Baker, B., Saylor, R. D., and Montuoro, R.:
751 Harmonized Emissions Component (HEMCO) 3.0 as a versatile emissions component for
752 atmospheric models: application in the GEOS-Chem, NASA GEOS, WRF-GC, CESM2,
753 NOAA GEFS-Aerosol, and NOAA UFS models, *Geosci. Model Dev.*, 14, 5487-5506,
754 10.5194/gmd-14-5487-2021, 2021.

755 Lin, J. T., and McElroy, M. B.: Detection from space of a reduction in anthropogenic emissions
756 of nitrogen oxides during the Chinese economic downturn, *Atmos. Chem. Phys.*, 11, 8171-
757 8188, 10.5194/acp-11-8171-2011, 2011.

758 Messina, P., Lathièrè, J., Sindelarova, K., Vuichard, N., Granier, C., Ghattas, J., Cozic, A., and
759 Hauglustaine, D. A.: Global biogenic volatile organic compound emissions in the
760 ORCHIDEE and MEGAN models and sensitivity to key parameters, *Atmos. Chem. Phys.*,
761 16, 14169-14202, 10.5194/acp-16-14169-2016, 2016.

762 Miyazaki, K., Bowman, K., Sekiya, T., Eskes, H., Boersma, F., Worden, H., Livesey, N.,
763 Payne, V. H., Sudo, K., Kanaya, Y., Takigawa, M., and Ogochi, K.: Updated tropospheric
764 chemistry reanalysis and emission estimates, TCR-2, for 2005–2018, *Earth Syst. Sci. Data*,
765 12, 2223-2259, 10.5194/essd-12-2223-2020, 2020.

766 Müller, J. F., Stavrou, T., Bauwens, M., George, M., Hurtmans, D., Coheur, P. F., Clerbaux,
767 C., and Sweeney, C.: Top-Down CO Emissions Based On IASI Observations and
768 Hemispheric Constraints on OH Levels, *Geophys. Res. Lett.*, 45, 1621-1629,
769 10.1002/2017gl076697, 2018.

770 Page, S., Hoscilo, A., Langner, A., Tansey, K., Siegert, F., Limin, S., and Rieley, J.: Tropical
771 peatland fires in Southeast Asia, in: *Tropical Fire Ecology: Climate Change, Land Use, and*
772 *Ecosystem Dynamics*, edited by: Cochrane, M. A., Springer Praxis Books, Springer, Berlin,
773 Heidelberg, 2009.

774 Qu, Z., Henze, D. K., Worden, H. M., Jiang, Z., Gaubert, B., Theys, N., and Wang, W.: Sector-
775 based top-down estimates of NO_x, SO₂, and CO emissions in East Asia, *Geophys. Res. Lett.*,
776 49, e2021GL096009, 10.1029/2021gl096009, 2022.

777 Smoydzin, L., and Hoor, P.: Contribution of Asian emissions to upper tropospheric CO over
778 the remote Pacific, *Atmos. Chem. Phys.*, 22, 7193-7206, 10.5194/acp-22-7193-2022, 2022.

779 Tan, H., Zhang, L., Lu, X., Zhao, Y., Yao, B., Parker, R. J., and Boesch, H.: An integrated
780 analysis of contemporary methane emissions and concentration trends over China using in
781 situ and satellite observations and model simulations, *Atmos. Chem. Phys.*, 22, 1229-1249,
782 10.5194/acp-22-1229-2022, 2022.

783 Tang, W., Arellano, A. F., Gaubert, B., Miyazaki, K., and Worden, H. M.: Satellite data reveal
784 a common combustion emission pathway for major cities in China, *Atmos. Chem. Phys.*, 19,
785 4269-4288, 10.5194/acp-19-4269-2019, 2019.

786 Tang, W., Gaubert, B., Emmons, L., Ziskin, D., Mao, D., Edwards, D., Arellano, A., Raeder,
787 K., Anderson, J., and Worden, H.: Advantages of assimilating multispectral satellite retrievals
788 of atmospheric composition: a demonstration using MOPITT carbon monoxide products,
789 *Atmos. Meas. Tech.*, 17, 1941-1963, 10.5194/amt-17-1941-2024, 2024.

790 Tang, Z., Chen, J., and Jiang, Z.: Discrepancy in assimilated atmospheric CO over East Asia
791 in 2015–2020 by assimilating satellite and surface CO measurements, *Atmos. Chem. Phys.*,
792 22, 7815-7826, 10.5194/acp-22-7815-2022, 2022.

793 Tang, Z., Jiang, Z., Chen, J., Yang, P., and Shen, Y.: The capabilities of the adjoint of GEOS-
794 Chem model to support HEMCO emission inventories and MERRA-2 meteorological data,
795 *Geosci. Model Dev.*, 16, 6377-6392, 10.5194/gmd-16-6377-2023, 2023.

796 Todling, R., and Cohn, S. E.: Suboptimal schemes for atmospheric data assimilation based on
797 the Kalman filter, *Monthly Weather Review*, 122, 10.1175/1520-
798 0493(1994)122<2530:SSFADA>2.0.CO;2, 1994.

799 Tong, D., Pan, L., Chen, W., Lamsal, L., Lee, P., Tang, Y., Kim, H., Kondragunta, S., and
800 Stajner, I.: Impact of the 2008 Global Recession on air quality over the United States:
801 Implications for surface ozone levels from changes in NO_x emissions, *Geophys. Res. Lett.*,
802 43, 9280-9288, 10.1002/2016gl069885, 2016.

803 van der Werf, G. R., Randerson, J. T., Giglio, L., Collatz, G. J., Mu, M., Kasibhatla, P. S.,
804 Morton, D. C., DeFries, R. S., Jin, Y., and van Leeuwen, T. T.: Global fire emissions and the
805 contribution of deforestation, savanna, forest, agricultural, and peat fires (1997–2009),
806 *Atmos. Chem. Phys.*, 10, 11707-11735, 10.5194/acp-10-11707-2010, 2010.

807 van der Werf, G. R., Randerson, J. T., van Wees, D., Chen, Y., Giglio, L., Hall, J., Vernooij,
808 R., Mu, M., Binte Shahid, S., Barsanti, K. C., Yokelson, R., and Morton, D. C.: Landscape
809 fire emissions from the 5(th) version of the Global Fire Emissions Database (GFED5), *Sci*
810 *Data*, 12, 1870, 10.1038/s41597-025-06127-w, 2025.

811 Warner, J., Carminati, F., Wei, Z., Lahoz, W., and Attié, J. L.: Tropospheric carbon monoxide
812 variability from AIRS under clear and cloudy conditions, *Atmos. Chem. Phys.*, 13, 12469-
813 12479, 10.5194/acp-13-12469-2013, 2013.

814 Whaley, C. H., Strong, K., Jones, D. B. A., Walker, T. W., Jiang, Z., Henze, D. K., Cooke, M.
815 A., McLinden, C. A., Mittermeier, R. L., Pommier, M., and Fogal, P. F.: Toronto area ozone:
816 Long-term measurements and modeled sources of poor air quality events, *J. Geophys. Res.-*
817 *Atmos.*, 120, 11368-11390, 10.1002/2014JD022984, 2015.

818 Wofsy, S. C., and HIPPO Science Team: HIAPER Pole-to-Pole Observations (HIPPO): fine-
819 grained, global-scale measurements of climatically important atmospheric gases and aerosols,
820 *Philosophical Transactions of the Royal Society A: Mathematical, Physical and Engineering*
821 *Sciences*, 369, 2073-2086, 10.1098/rsta.2010.0313, 2011.

822 Wofsy, S. C., and Atom Science Team: ATom: Aircraft Flight Track and Navigational Data.
823 ORNL DAAC, Oak Ridge, Tennessee, USA. , 10.3334/ORNLDAAAC/1613, 2018.

824 Worden, H. M., Deeter, M. N., Edwards, D. P., Gille, J. C., Drummond, J. R., and Nédélec, P.:
825 Observations of near-surface carbon monoxide from space using MOPITT multispectral
826 retrievals, *J. Geophys. Res.-Atmos.*, 115, D18314, 10.1029/2010jd014242, 2010.

827 Worden, H. M., Deeter, M. N., Frankenberg, C., George, M., Nichitiu, F., Worden, J., Aben,
828 I., Bowman, K. W., Clerbaux, C., Coheur, P. F., de Laat, A. T. J., Detweiler, R., Drummond,
829 J. R., Edwards, D. P., Gille, J. C., Hurtmans, D., Luo, M., Martínez-Alonso, S., Massie, S.,
830 Pfister, G., and Warner, J. X.: Decadal record of satellite carbon monoxide observations,
831 *Atmos. Chem. Phys.*, 13, 837-850, 10.5194/acp-13-837-2013, 2013.

832 Worden, J. R., Bloom, A. A., Pandey, S., Jiang, Z., Worden, H. M., Walker, T. W., Houweling,
833 S., and Rockmann, T.: Reduced biomass burning emissions reconcile conflicting estimates of
834 the post-2006 atmospheric methane budget, *Nat. Commun.*, 8, 2227, 10.1038/s41467-017-
835 02246-0, 2017.

836 Xia, Y., Zhao, Y., and Nielsen, C. P.: Benefits of China's efforts in gaseous pollutant control
837 indicated by the bottom-up emissions and satellite observations 2000–2014, *Atmos. Environ.*,
838 136, 43-53, 10.1016/j.atmosenv.2016.04.013, 2016.

839 Zhao, Y., Nielsen, C. P., McElroy, M. B., Zhang, L., and Zhang, J.: CO emissions in China:
840 Uncertainties and implications of improved energy efficiency and emission control, *Atmos.*
841 *Environ.*, 49, 103-113, 10.1016/j.atmosenv.2011.12.015, 2012.

842 Zhao, Y., Saunio, M., Bousquet, P., Lin, X., Berchet, A., Hegglin, M. I., Canadell, J. G.,
843 Jackson, R. B., Deushi, M., Jöckel, P., Kinnison, D., Kirner, O., Strode, S., Tilmes, S.,
844 Dlugokencky, E. J., and Zheng, B.: On the role of trend and variability in the hydroxyl radical
845 (OH) in the global methane budget, *Atmos. Chem. Phys.*, 20, 13011-13022, 10.5194/acp-20-
846 13011-2020, 2020.

847 Zheng, B., Chevallier, F., Yin, Y., Ciais, P., Fortems-Cheiney, A., Deeter, M. N., Parker, R. J.,
848 Wang, Y., Worden, H. M., and Zhao, Y.: Global atmospheric carbon monoxide budget 2000–
849 2017 inferred from multi-species atmospheric inversions, *Earth Syst. Sci. Data*, 11, 1411-
850 1436, 10.5194/essd-11-1411-2019, 2019.

851 Zheng, B., Ciais, P., Chevallier, F., Chuvieco, E., Chen, Y., and Yang, H.: Increasing forest
852 fire emissions despite the decline in global burned area, *Sci. Adv.*, 7, eabh2646,
853 10.1126/sciadv.abh2646, 2021.

854 Zheng, B., Ciais, P., Chevallier, F., Yang, H., Canadell, J. G., Chen, Y., van der Velde, I. R.,
855 Aben, I., Chuvieco, E., Davis, S. J., Deeter, M., Hong, C., Kong, Y., Li, H., Li, H., Lin, X.,
856 He, K., and Zhang, Q.: Record-high CO₂ emissions from boreal fires in 2021, *Science*, 379,
857 912-917, 10.1126/science.ade0805, 2023.

858 Zhu, C., Byrd, R. H., Lu, P., and Nocedal, J.: Algorithm 778: L-BFGS-B: Fortran Subroutines
859 for Large-Scale Bound Constrained Optimization, *ACM Transactions on Mathematical*
860 *Software*, 23, 550-560, 10.1145/279232.279236, 1997.

861

Observations	GC-original	GC-a priori	Column-FixOH	Profile-FixOH	Column-VarOH
MOPITT	-39.4	-9.7	-7.3	-6.8	-5.1
WDGCG	-18.3	-1.4	1.8	1.9	0.3
HIPPO	-18.9	-3.8	-2.5	-2.1	-2.2
ATOM	-16.2	-3.4	-2.1	-2.9	-1.6

Table 1. Mean biases of modeled CO concentrations relative to satellite (MOPITT) and in-situ (WDCGG, HIPPO, ATom) observations for five model simulations over the period 2003-2022. Biases are in units of 10^{16} molec cm^{-2} for MOPITT and ppb for other datasets.

Anthropogenic emissions		US	Europe	E. China	India	SE. Asia	Global
GC-a priori	Emissions	53.5	33.7	179.6	72.7	26.1	536.3
	Trends	-1.8 ± 0.1	-0.7 ± 0.1	-1.4 ± 0.3	0.3 ± 0.1	0.1 ± 0.0	-3.6 ± 0.4
Column-FixOH	Emissions	61.6	39.2	195.8	73.3	26.9	612.8
	Trends	-2.2 ± 0.3	-0.9 ± 0.2	-4.0 ± 0.8	0.8 ± 0.3	0.0 ± 0.1	-5.6 ± 0.9
Profile-FixOH	Emissions	56.7	36.3	188.3	69.9	26.8	572.2
	Trends	-2.0 ± 0.3	-0.8 ± 0.2	-3.0 ± 0.4	0.5 ± 0.2	0.1 ± 0.1	-5.0 ± 0.4
Column-VarOH	Emissions	58.2	38.5	186.7	67.7	26.3	590.1
	Trends	-2.0 ± 0.3	-0.9 ± 0.2	-3.7 ± 0.8	0.7 ± 0.2	-0.0 ± 0.1	-5.3 ± 0.8

Table 2. Mean anthropogenic CO emissions (Tg yr^{-1}) and their trends (Tg yr^{-2}) in 2003-2022: A comparison of a priori inventories with those constrained by MOPITT retrievals under different configurations. The region definition is shown in Figure S1e.

Biomass burning		Boreal N. America	Boreal Asia	S. America	Africa	SE. Asia	Australia	Global
GC-a priori	Emissions	21.5	39.5	44.0	136.9	25.0	12.0	312.5
	Trends	1.1 ± 1.1	1.3 ± 1.8	-0.6 ± 1.7	-1.4 ± 0.5	-0.8 ± 1.6	-0.0 ± 0.6	-0.6 ± 3.2
Column-FixOH	Emissions	20.4	45.4	37.4	167.5	18.0	15.1	345.6
	Trends	0.6 ± 1.3	1.6 ± 1.9	-0.9 ± 1.4	0.5 ± 0.8	-0.5 ± 0.8	-0.2 ± 0.6	0.9 ± 3.4
Profile-FixOH	Emissions	21.2	46.7	38.4	148.8	19.7	13.7	326.6
	Trends	1.1 ± 1.5	2.1 ± 2.7	-1.1 ± 1.4	0.3 ± 0.8	-0.6 ± 1.1	-0.1 ± 0.6	1.7 ± 4.4
Column-VarOH	Emissions	18.0	41.0	33.3	159.5	19.0	15.8	325.7
	Trends	0.3 ± 0.8	1.1 ± 1.6	-1.0 ± 1.2	0.1 ± 0.8	-0.1 ± 0.8	0.1 ± 0.5	-0.1 ± 2.4

Table 3. Mean biomass burning CO emissions (Tg yr^{-1}) and their trends (Tg yr^{-2}) in 2003-2022: A comparison of a priori inventories (GFED4) with those constrained by MOPITT retrievals under different configurations. The region definition is shown in Figure S1f.

Region	Anthropogenic	Region	Biomass burning
United States	-0.57 ± 0.11	Boreal N. America	0.43 ± 0.49
Europe	-0.69 ± 0.09	Boreal Asia	0.48 ± 0.53
Eastern China	-0.69 ± 0.22	South America	-0.13 ± 0.27
India	0.03 ± 0.16	Africa	0.09 ± 0.19
Southeast Asia	-0.19 ± 0.18	Southeast Asia	-0.22 ± 0.41
\	\	Australia	-0.12 ± 0.22
Northern Hemisphere	-0.51 ± 0.12	Northern Hemisphere	0.24 ± 0.33
Global	-0.27 ± 0.11	Global	0.10 ± 0.25

Table 4. Attribution of trends in column CO concentrations ($\% \text{ yr}^{-1}$) from 2003 to 2022 to changes in anthropogenic and biomass burning emissions, based on sensitivity simulations using the Column-FixOH inversion results.

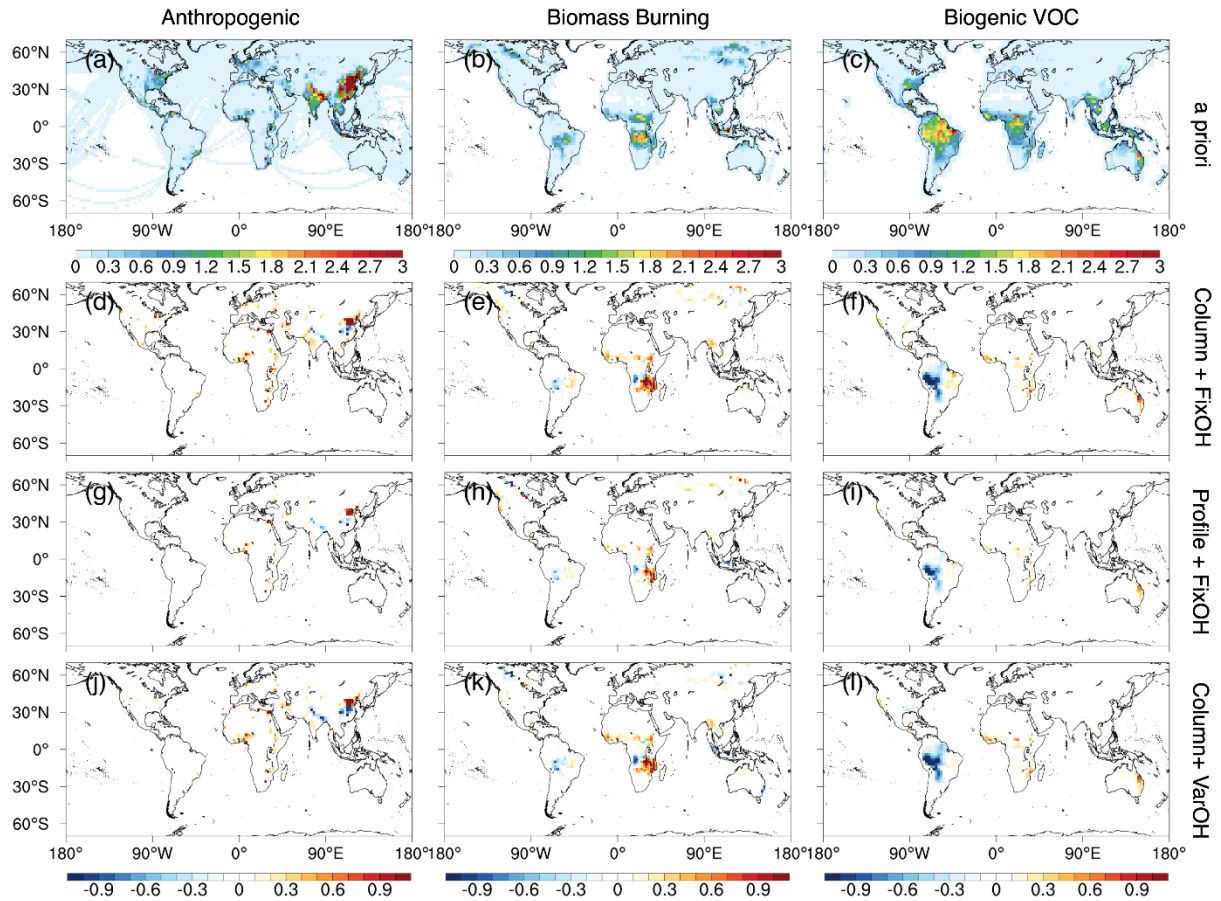


Fig. 1. Spatial patterns of a priori CO emissions and a posteriori emission scaling factors for the period 2003-2022. (a-c) Mean a priori CO emissions ($10^{12} \text{ molec cm}^{-2} \text{ s}^{-1}$). (d-l) Scaling factors (ratio of a posteriori to a priori emissions) derived from the three inversion experiments: (d-f) Column-FixOH, (g-i) Profile-FixOH, and (j-l) Column-VarOH.

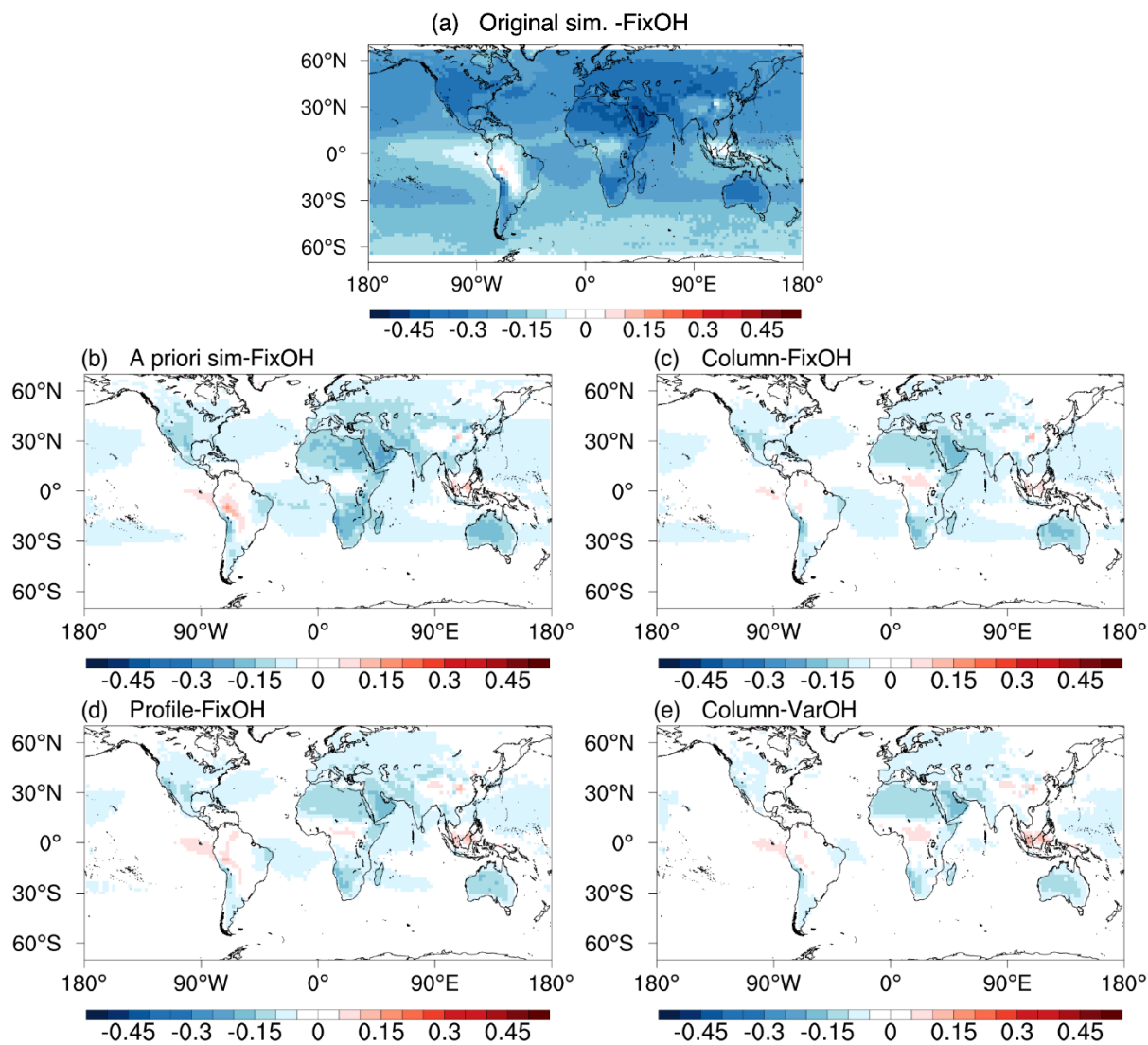


Fig. 2. Relative bias in column CO for 2003-2022, calculated as $(\text{Model} - \text{MOPITT}) / \text{MOPITT}$ for GC-original (a), GC-a priori (b), and a posteriori simulations (c-e).

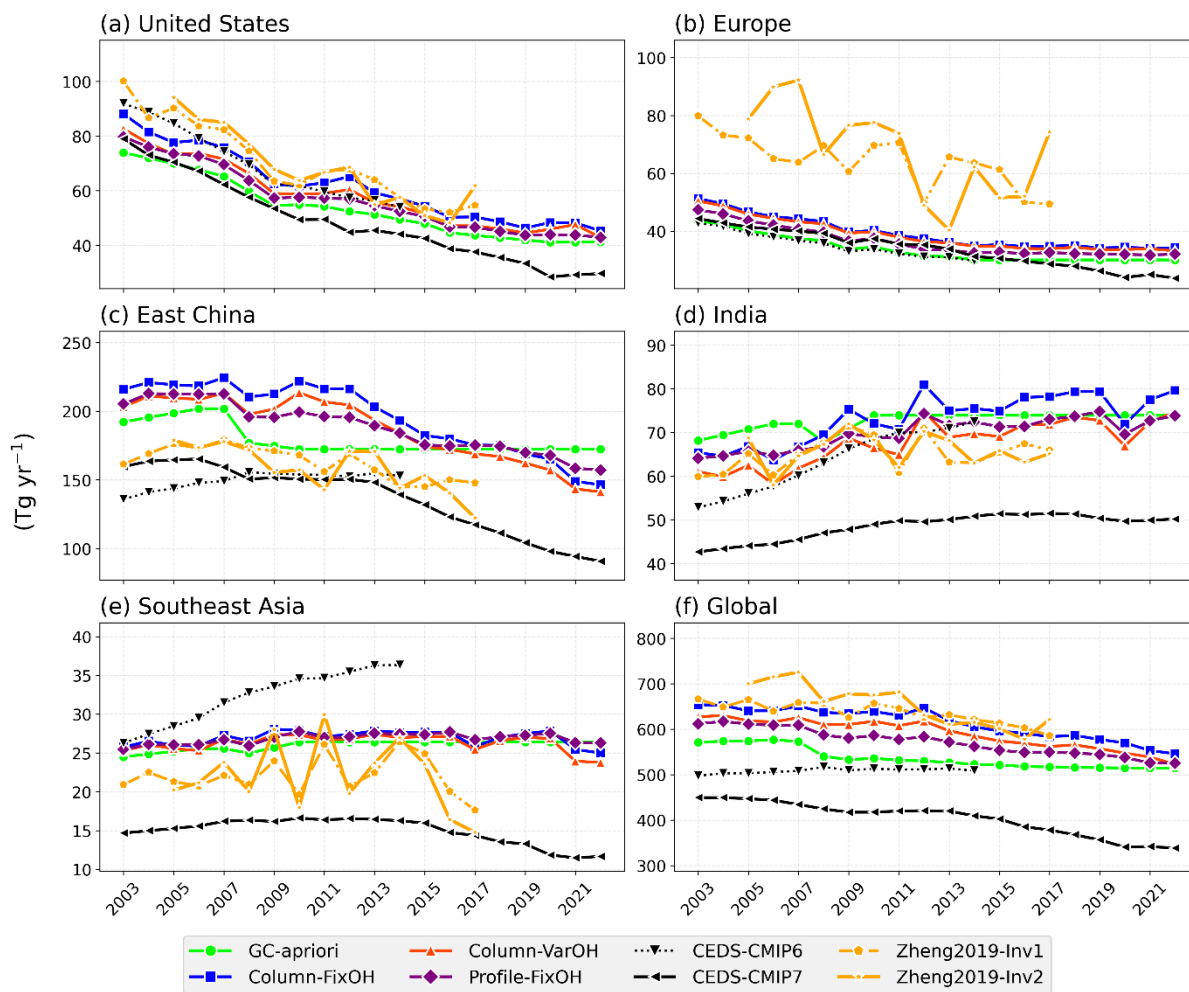


Fig. 3. Time series of anthropogenic CO emissions from 2003 to 2022 across major regions, comparing a priori inventories, a posteriori inversions from this study, and independent estimates from CEDS-CMIP6/7 and Zheng et al. (2019).

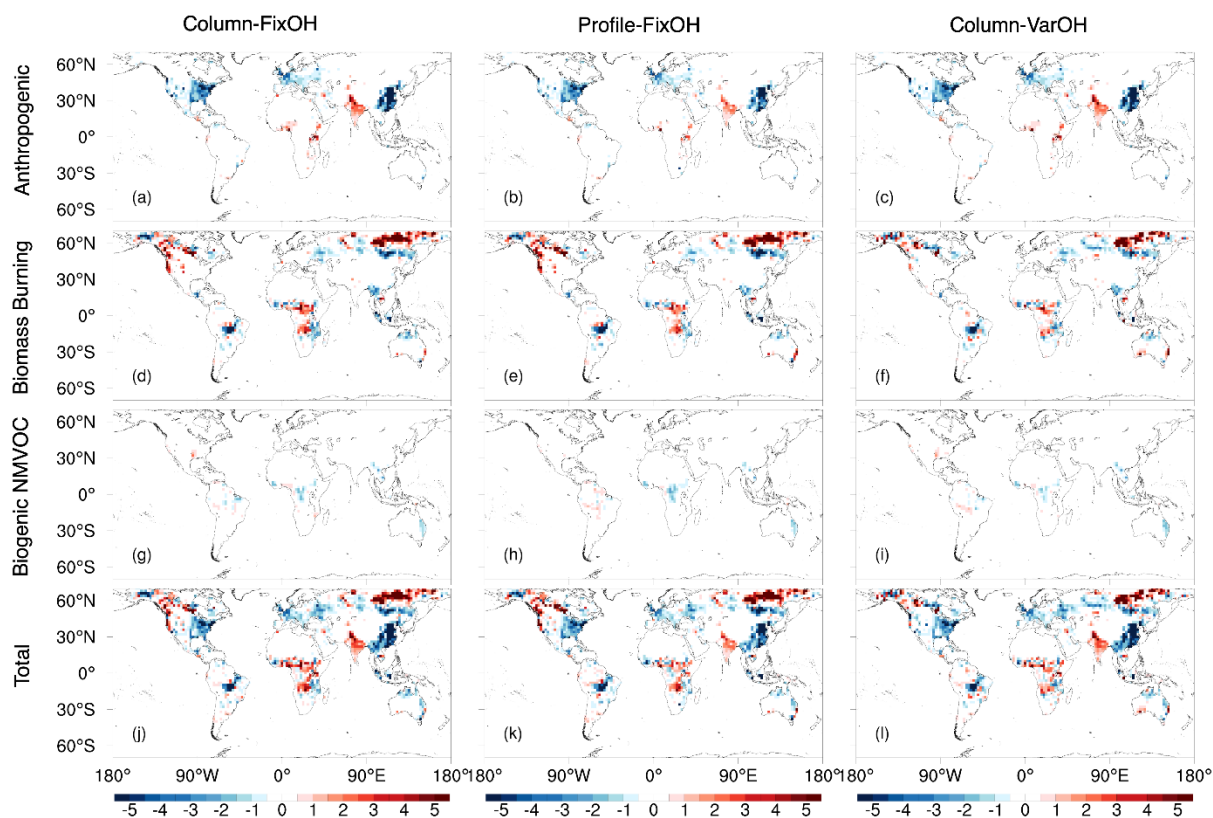


Fig. 4. Long-term trends in CO emissions ($10^{10} \text{ molec cm}^{-2} \text{ s}^{-1} \text{ yr}^{-1}$) from different sources (2003-2022) as constrained by the three inversion experiments. For anthropogenic and biogenic VOC trends, months dominated by biomass burning (>50% contribution) were excluded in this figure. This approach ensures that the derived trends more accurately reflect the actual changes in anthropogenic and biogenic VOC emissions, without being biased by short-term, seasonal biomass burning signals.

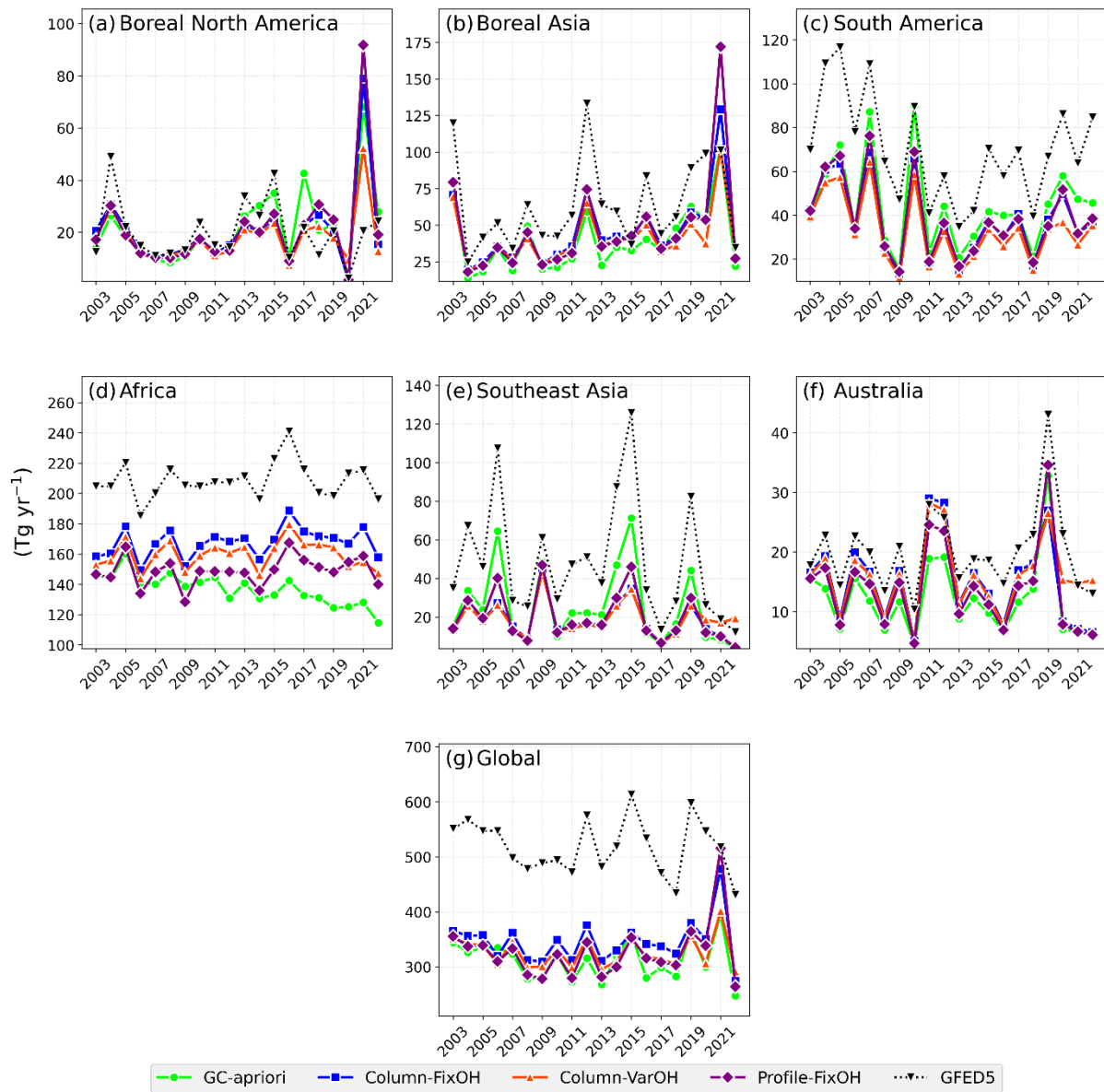


Fig. 5. Time series of biomass burning CO emissions from 2003 to 2022, comparing the a priori inventory (GFED4), a posteriori inversions, and the GFED5 inventory.

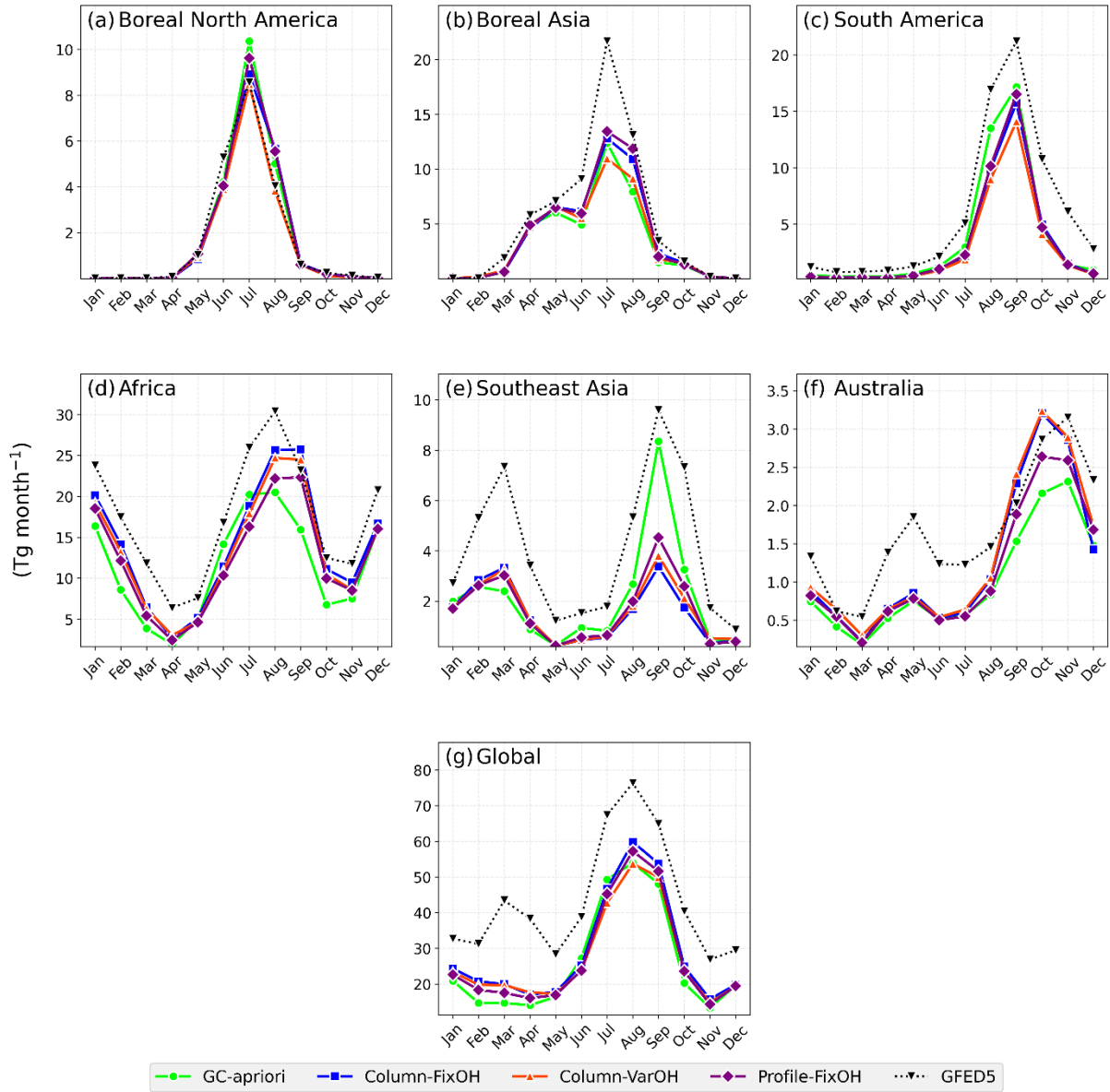


Fig. 6. Climatological monthly cycle (2003-2022 average) of biomass burning CO emissions across different regions, comparing a priori (GFED4) and a posteriori estimates with GFED5.

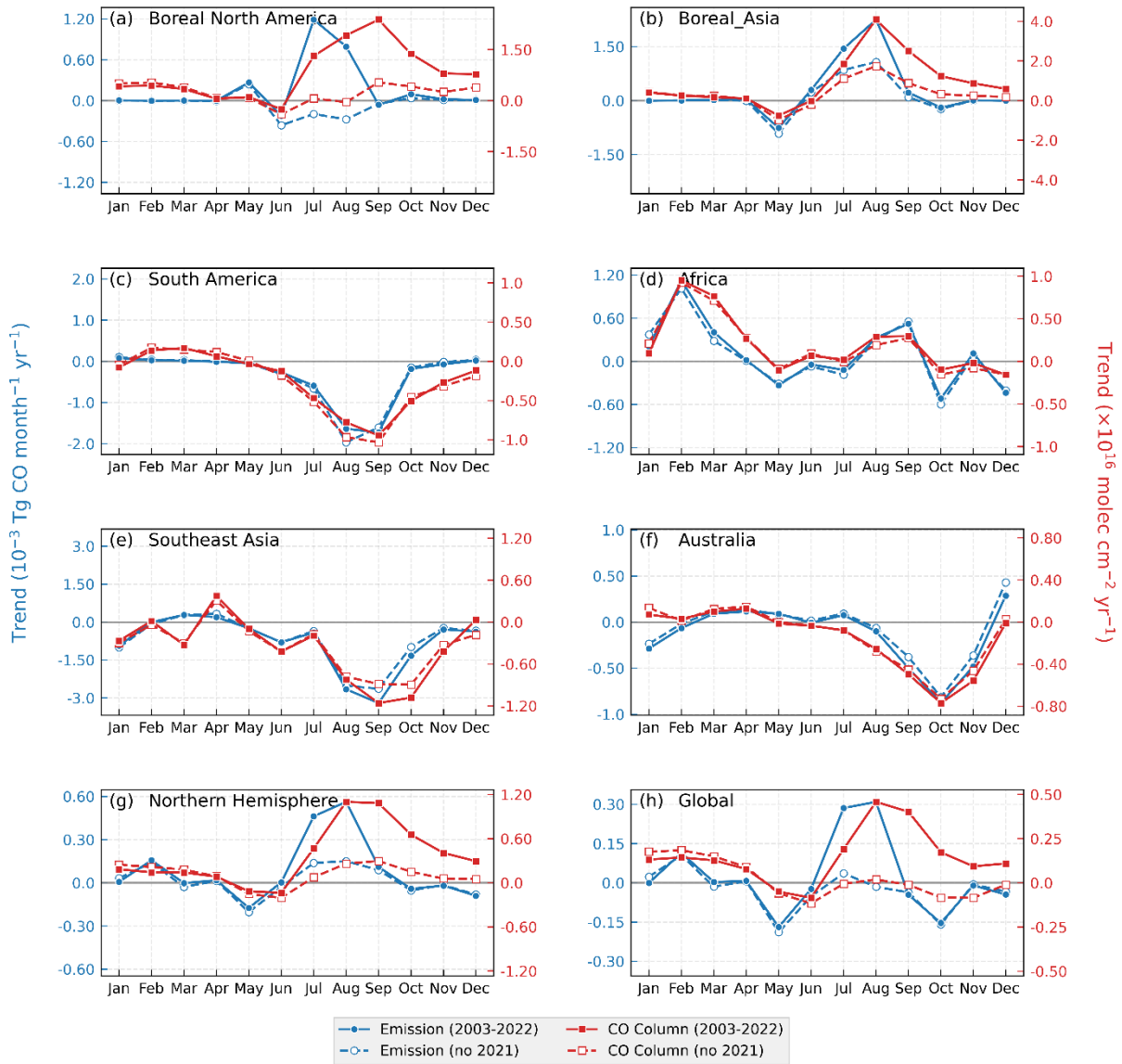


Fig. 7. Monthly trends in biomass burning CO emissions (based on Column-FixOH) and their impact on column CO concentrations (2003-2022). Solid lines show trends including 2021, while dashed lines exclude 2021 to illustrate the impact of extreme fire year. Please check Fig. S4 and S5 for the standard deviation of the trends.

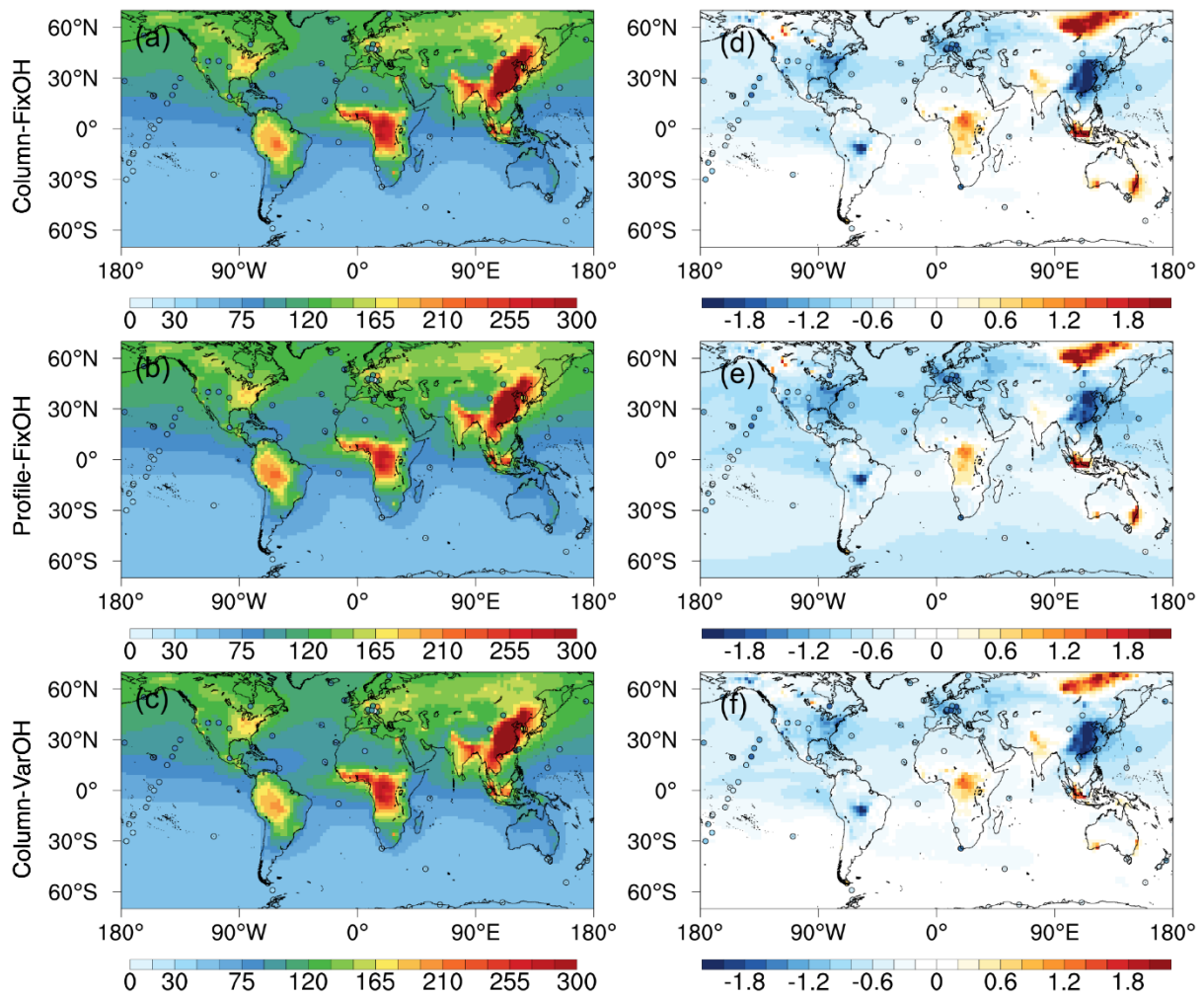


Fig. 8. Modeled surface CO concentrations (ppb) and their trends ($\% \text{ yr}^{-1}$) from 2003 to 2022. (a-c) Mean concentrations from WDCGG observations and model simulations. (d-f) Spatial pattern of the long-term trend. Only stations with 14 year observations (the time range between the first and last observations) during 2003-2022 are included.

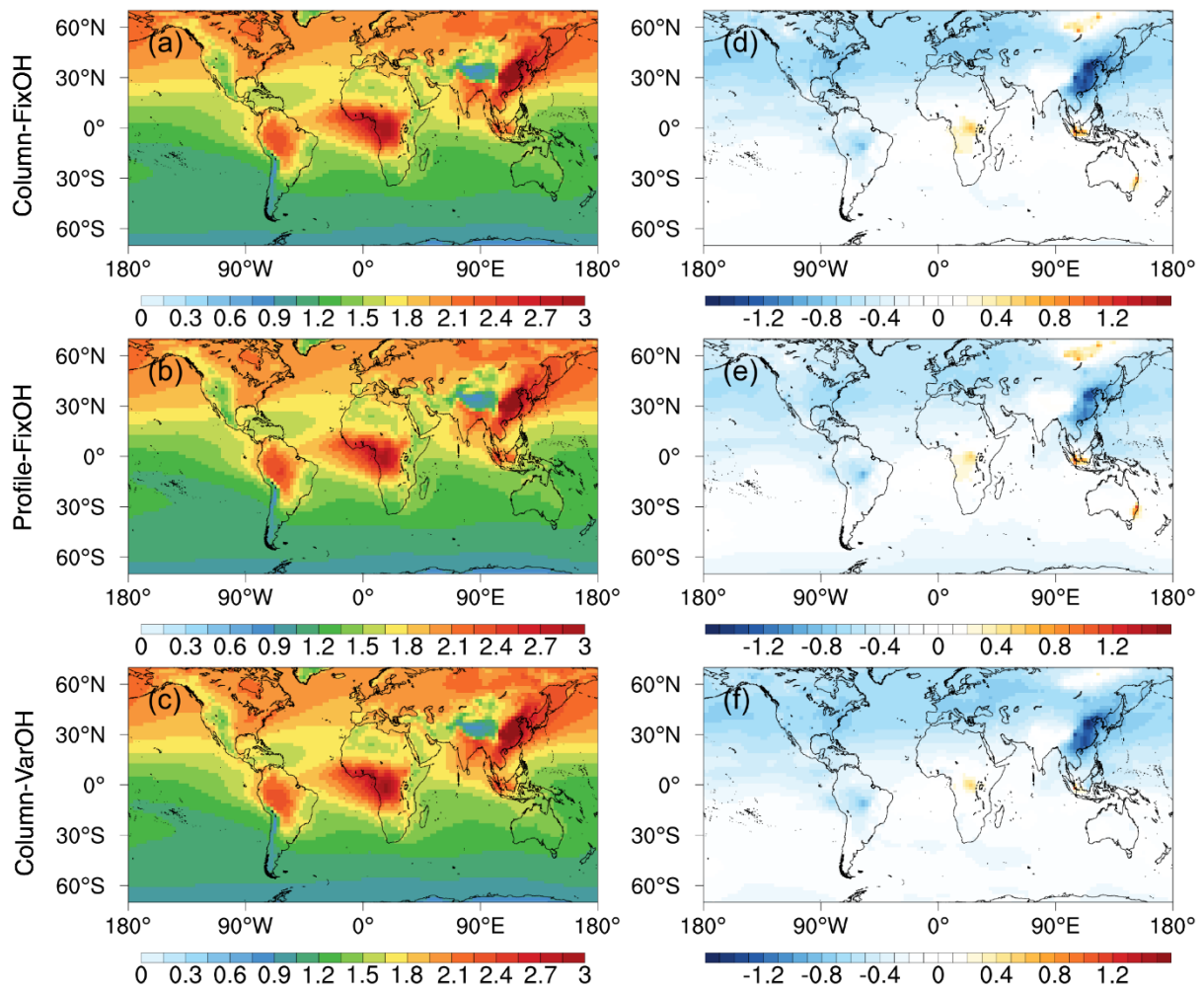


Fig. 9. Modeled column CO concentrations (10^{18} molec cm^{-2}) and their trends ($\% \text{ yr}^{-1}$) from 2003 to 2022. (a-c) Spatial distribution of the 20-year mean. (d-f) Spatial pattern of the long-term trend.

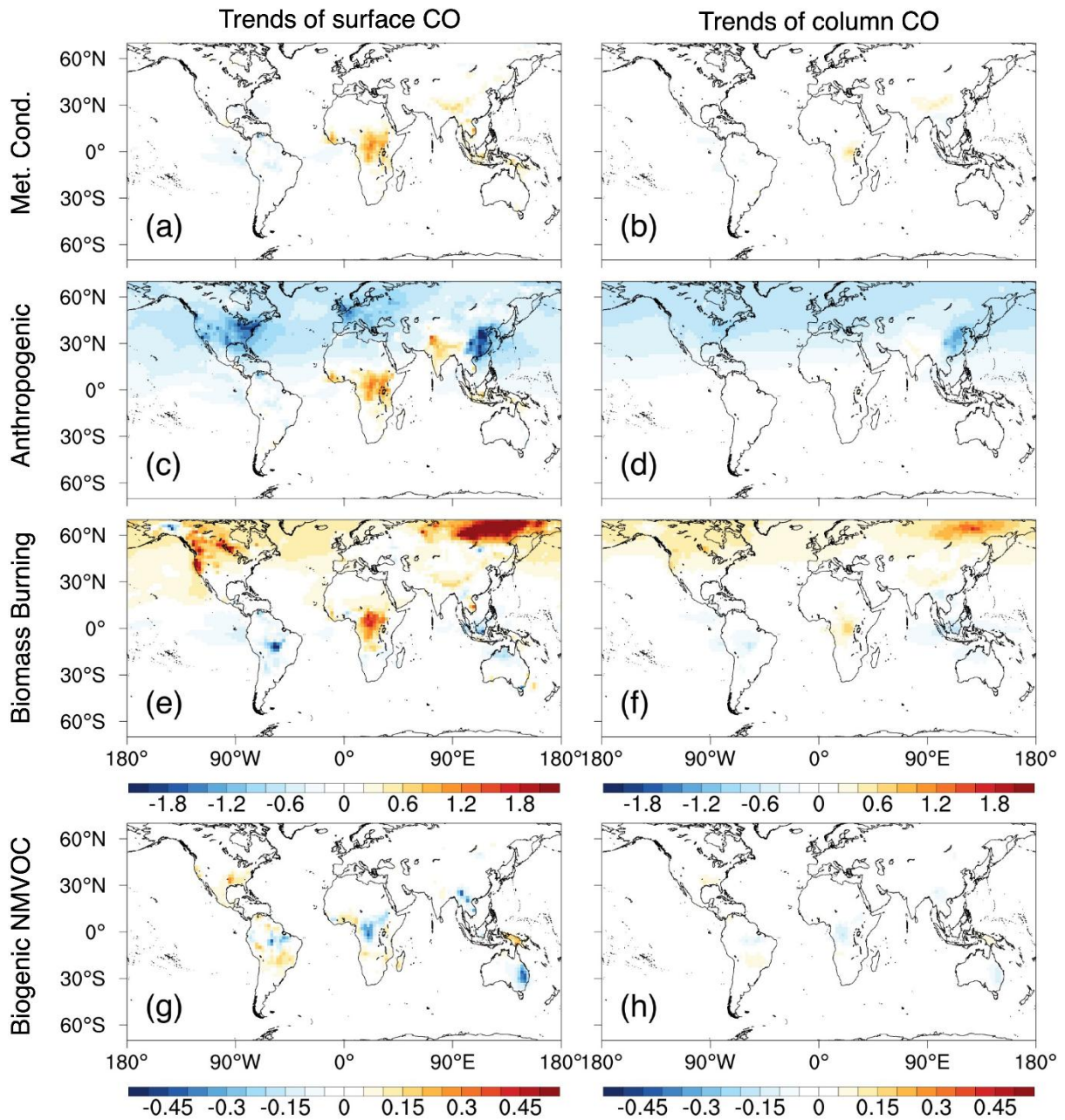


Fig. 10. Attribution of trends ($\% \text{ yr}^{-1}$) in surface and column CO concentrations to individual drivers, derived from sensitivity simulations based on Column-FixOH inversion (2003-2022). Trends are shown for scenarios with: (a, b) all emissions fixed at 2003 levels; (c, d) only anthropogenic emissions varying over time; (e, f) only biomass burning emissions varying; (g, h) only biogenic VOC emissions varying.

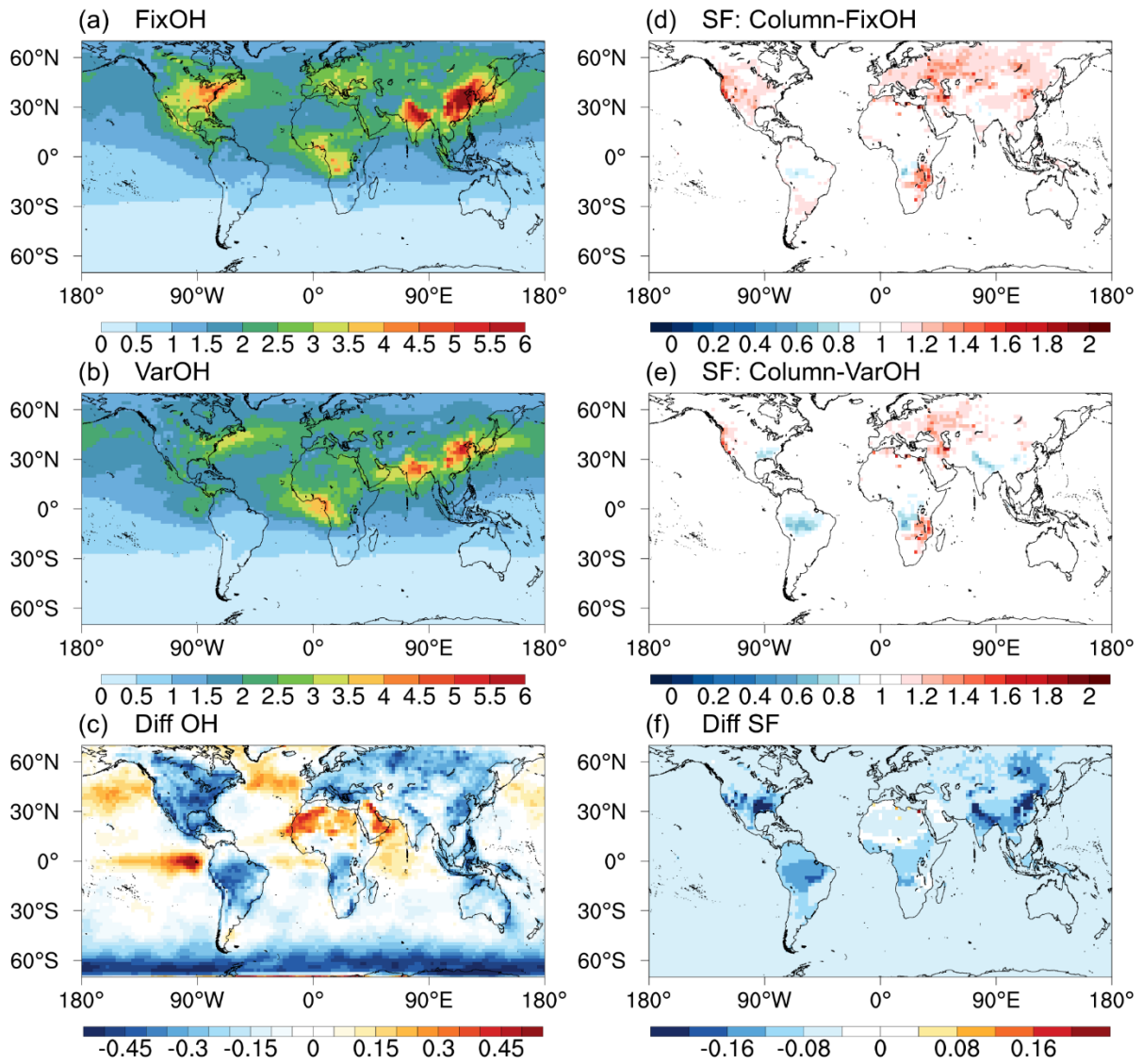


Fig. 11. Sensitivity of inverted CO emissions to OH fields. (a-c) Tropospheric OH columns (10^{12} molec cm^{-2}) from fixed and variable (TCR-2) fields and their difference. (d-f) Corresponding scaling factors from the Column-FixOH and Column-VarOH inversions and their difference. Please note that due to the use of land boundary conditions, differences in OH concentrations over the ocean in the left column figures have a negligible effect on the differences in scaling factors shown in the right column figures.